JCB Journal of Cell Biology

ARTICLE

LET-767 determines lipid droplet protein targeting and lipid homeostasis

Lin Fu[1*], Jingjing Zhang[1*], Yanli Wang[1*], Huiyin Wu[1*], Xiumei Xu[1], Chunxia Li[1], Jirong Li[1], Jing Liu[1], Haizhen Wang[4], Xue Jiang[8], Zhihao Li[1], Yaomei He[1], Pingsheng Liu[7], Yingjie Wu[5,6], Xiaoju Zou[3], and Bin Liang[1,2]

Lipid droplets (LDs) are composed of a core of neutral lipids wrapped by a phospholipid (PL) monolayer containing several hundred proteins that vary between different cells or organisms. How LD proteins target to LDs is still largely unknown. Here, we show that RNAi knockdown or gene mutation of *let-767*, encoding a member of hydroxysteroid dehydrogenase (HSD), displaced the LD localization of three well-known LD proteins: DHS-3 (dehydrogenase/reductase), PLIN-1 (perilipin), and DGAT-2 (diacylglycerol O-acyltransferase 2), and also prevented LD growth in *Caenorhabditis elegans*. LET-767 interacts with ARF-1 (ADP-ribosylation factor 1) to prevent ARF-1 LD translocation for appropriate LD protein targeting and lipid homeostasis. Deficiency of LET-767 leads to the release of ARF-1, which further recruits and promotes translocation of ATGL-1 (adipose triglyceride lipase) to LDs for lipolysis. The displacement of LD proteins caused by LET-767 deficiency could be reversed by inhibition of either ARF-1 or ATGL-1. Our work uncovers a unique LET-767 for determining LD protein targeting and maintaining lipid homeostasis.

Introduction

Lipid droplets (LDs) are neutral lipid storage organelles that conventionally function as hubs of cellular lipid and energy metabolism. They are involved in regulation of gene expression (Gallardo-Montejano et al., 2016; Mejhert et al., 2020), histone sequestration (Cermelli et al., 2006), viral replication (Miyanari et al., 2007), drug activity (Greenwood et al., 2019), and so on. Either overproduction or underproduction of LDs has been implicated in the etiology of human diseases, especially metabolic disorders such as obesity, fatty liver, type 2 diabetes, cardiovascular diseases, as well as others (Zadoorian et al., 2023). Therefore, LD homeostasis must be tightly regulated to ensure its appropriate functions.

LDs have a unique architecture consisting of a core of neutral lipids, mostly triacylglycerols (TAGs) or sterol esters, encircled by a phospholipid (PL) monolayer decorated with tens to hundreds of proteins (LD proteins) that vary among species and cell types as shown by various proteomics-based approaches. The functions of LDs are regulated by these LD proteins, which represent a variety of functional classes, such as lipid metabolism, membrane trafficking, and protein degradation (Bartz et al., 2007; Bersuker and Olzmann, 2017; Fujimoto et al., 2004; Gao et al., 2019; Vrablik et al., 2015; Zhang and Liu, 2019; Zhang et al., 2012). How LD proteins recognize and localize to LD surfaces to function is one of the key aspects of cell biology. Based on their trafficking pathways, LD proteins are generally classified into two major and distinct classes: Class I LD proteins are first inserted into the endoplasmic reticulum (ER) membrane and then relocalized to the LD surface (ERTOLD), while Class II LD proteins are initially translated in the cytosol (Cyto) and subsequently recruited to the LD surface (CYTOLD) (Kory et al., 2016; Olarte et al., 2022).

Class I LD proteins are generally thought to adopt a hairpin conformation in which a hydrophobic domain embedded in the monolayer is flanked by hydrophilic regions that are exposed to the Cyto, forming a V shape extending from the membrane, either during LD formation or after formation via ER-LD

[1]Center for Life Sciences, Yunnan Key Laboratory of Cell Metabolism and Diseases, School of Life Sciences, Yunnan University, Kunming, China; [2]Southwest United Graduate School, Kunming, China; [3]College of Chinese Materia Medica and Yunnan Key Laboratory of Southern Medicinal Utilization, Yunnan University of Chinese Medicine, Kunming, China; [4]College of Veterinary Medicine, Yunnan Agricultural University, Kunming, China; [5]School of Laboratory Animal and Shandong Laboratory Animal Center, Science and Technology Innovation Center, Shandong First Medical University and Shandong Academy of Medical Sciences, Jinan, China; [6]Institute for Genome Engineered Animal Models of Human Diseases, National Center of Genetically Engineered Animal Models for International Research, Liaoning Provence Key Lab of Genome Engineered Animal Models Dalian Medical University, Dalian, China; [7]National Laboratory of Biomacromolecules, Institute of Biophysics, Chinese Academy of Sciences, Beijing, China; [8]Key Laboratory of Animal Models and Human Disease Mechanisms of the Chinese Academy of Sciences and Yunnan province, Kunming Institute of Zoology, Center for Excellence in Animal Evolution and Genetics, Chinese Academy of Sciences, Kunming, China.

*L. Fu, J. Zhang, Y. Wang, and H. Wu contributed equally to this paper. Correspondence to Bin Liang: liangb73@ynu.edu.cn; Xiaoju Zou: xiaojuzou@163.com; Yingjie Wu: yjwu@sdfmu.edu.cn; Pingsheng Liu: pliu@ibp.ac.cn.

membrane bridges (Roberts and Olzmann, 2020). Examples of Class I LD proteins include the lipid biosynthesis enzymes glycerol-3-phosphate acyltransferase 4 (GPAT4) (Wilfling et al., 2013) and diacylglycerol O-acyltransferase 2 (DGAT2) (Stone et al., 2006), caveolin-1 (Ostermeyer et al., 2001) and caveolin-2 (Fujimoto et al., 2001), and HSD17B11 (Fujimoto et al., 2004; Yokoi et al., 2007), among others. Class II LD proteins often contain amphipathic helices with large hydrophobic residues, which detect and bind to the hydrophobic PL packing defects (Prévost et al., 2018). Examples of Class II proteins include the PLIN family (Blanchette-Mackie et al., 1995; Greenberg et al., 1991; Sztalryd and Brasaemle, 2017), the rate-limiting enzyme of phosphatidylcholine synthesis CTP: phosphocholine cytidylyltransferase (Krahmer et al., 2011), the LD–LD fusogenic protein CIDEA (Gong et al., 2011), and so on. Some class II proteins target LDs by binding to other LD proteins, such as hormone-sensitive lipase being recruited to LDs by perilipin 1 (Egan et al., 1992; Sztalryd et al., 2003). As well, fatty acid modification (conjugation of fatty acids such as myristate, palmitate, and isopentane to proteins) also provides a hydrophobic anchor that facilitates binding to PL membranes (Bartz et al., 2007; Suzuki et al., 2015). Altogether, the exact mechanism of these LD proteins targeting LDs for proper LD functionality is still largely unknown. Thus far, most studies on LD translocation have focused on the targeting motifs of LD proteins per se. It is unknown whether there are other pathways or specific proteins other than CYTOLD and ERTOLD required for LD protein targeting.

The genetically tractable organism *Caenorhabditis elegans* has conserved lipid metabolic pathways and stores neutral lipids in LDs mainly in the intestine and hypodermis (Watts and Ristow, 2017; Zhang et al., 2013). In *C. elegans*, several proteins such as DHS-3 (Zhang et al., 2012), DGAT-2 (Xu et al., 2012), PLIN-1/MDT-28 (Na et al., 2015), and ACS-4 (Vrablik et al., 2015) have been reported existing in LDs and have been used as marker proteins for LDs. We identified LET-767, a homologue of mammalian 17β-HSD3/12, required for both CYTOLD and ERTOLD pathway proteins, DHS-3, PLIN-1, and DGAT-2, targeting LDs. LET-767 is localized in both the ER and LDs and may function to prevent the LD translocation of ARF-1 and ATGL-1 for appropriate LD protein targeting and lipid homeostasis.

Results

RNAi reduction of LET-767 disrupted the targeting of LD proteins

LDs contain a core of neutral lipids wrapped by monolayer PLs decorated with LD proteins. The lipid dye LipidTOX stains the neutral lipids of LDs. DHS-3 is a short-chain dehydrogenase/reductase localized to LDs, and the DHS-3::GFP (Table S1) is a well-established LD marker that generally forms a ring encircling the LipidTOX-stained LDs in *C. elegans* (Na et al., 2015; Zhang et al., 2012). Therefore, we established an approach to identify genes or proteins required for the localization of DHS-3::GFP to LipidTOX-stained LDs (Fig. 1 A). We hypothesized that disruption of LD protein targeting may eventually result in altered LD size and lipid accumulation. Using RNAi knockdown, we screened 51 candidate genes in total (Table S2), including those affecting LD size in our previous screen (Zhang et al., 2021). Through this, we found that compared with the control (Con), RNAi knockdown of *let-767* resulted in smaller LDs (Fig. 1, B and C), similar to RNAi of *acs-1* (acetyl-CoA synthetase), but to a lesser extent as we previously reported (Zhang et al., 2021). More importantly, the green fluorescence of DHS-3::GFP was mostly displaced with the LipidTOX-stained LDs and displayed aggregation or diffusion in *let-767*RNAi worms (Fig. 1 D), suggesting that reduction of LET-767 probably affects the LD localization of DHS-3::GFP.

DHS-3 is a close homolog of 17β-HSD11 (Liu et al., 2018), which was reported to be mostly localized in the ER under normal conditions but concentrated on LDs under a certain condition (Yokoi et al., 2007). The SEL(1-79)::mCherry::HDEL (ER resident protein) and GFP::SP12 (ER resident protein signal peptidase) (Table S1) are two indicators for the ER (Zhang et al., 2021). The DHS-3::GFP and mCherry::HDEL displayed distinct fluorescence in Con worms, but mostly overlapped in *let-767*RNAi worms (Fig. 1, E and F), suggesting that the DHS-3::GFP may be retained in the ER under LET-767 reduction. A similar result was seen with DHS-3::mCherry and GFP::SP12 (Fig. 1, G and H). Thus, these results suggest that LET-767 is necessary for the translocation of DHS-3 from the ER to LDs.

Next, to test whether the regulation of LD targeting by LET-767 is specific for DHS-3 or also for other LD proteins, we examined another two well-known LD proteins in *C. elegans*. The perilipin protein PLIN-1/MDT-28 is a conserved LD protein in *C. elegans* and mammals (Na et al., 2015). Similar to DHS-3::mCherry, the PLIN-1::mCherry (Table S1) was also expressed in LDs as a ring structure in Con worms, while it was mostly retained in the ER in *let-767*RNAi worms (Fig. 1, I and J). DGAT-2 is a homolog of diacylglycerol O-acyltransferase 2 that incorporates fatty acids into diacylglycerol to biosynthesize TAG (Wu et al., 2018; Xu et al., 2012; Yang et al., 2022). As previously reported (Xu et al., 2012), similar to DHS-3::GFP/DHS-3::mCherry and PLIN-1::mCherry, the green fluorescence of GFP::DGAT-2 (Table S1) was localized to LDs as a ring structure in Con worms, but interestingly, it colocalized with Lyso tracker in *let-767*RNAi worms (Fig. 1, K and L), suggesting a displacement of DGAT-2. Taken all together, these lines of evidence indicate that LET-767 is essential for LD proteins correctly targeting LDs.

Genetic mutation of *let-767* consistently led to the dislocation of LD proteins

To verify the effect of LET-767 on LD protein targeting, we examined available and potential mutations of *let-767* from the *C. elegans* "million mutant project" (Table S1) (Thompson et al., 2013) (Fig. S1 A). Both Nile Red and LipidTOX staining of fixed worms fed on either an *E. coli HT115* diet or *OP50* diet showed that one (*gk553841*, M297V) out of seven mutations in *let-767* displayed significantly reduced LD size and lipid accumulation (Fig. S1, B–E). Similar to *let-767*RNAi but to a lesser extent, *let-767*(*gk553841*) worms also had decreased LD size and TAG content (Fig. 2, A–C), suggesting that this amino acid (M297) is essential for its function. We then crossed the DHS-3::GFP, DHS-3::mCherry, PLIN-1::mCherry, and GFP::DGAT-2 into *let-*

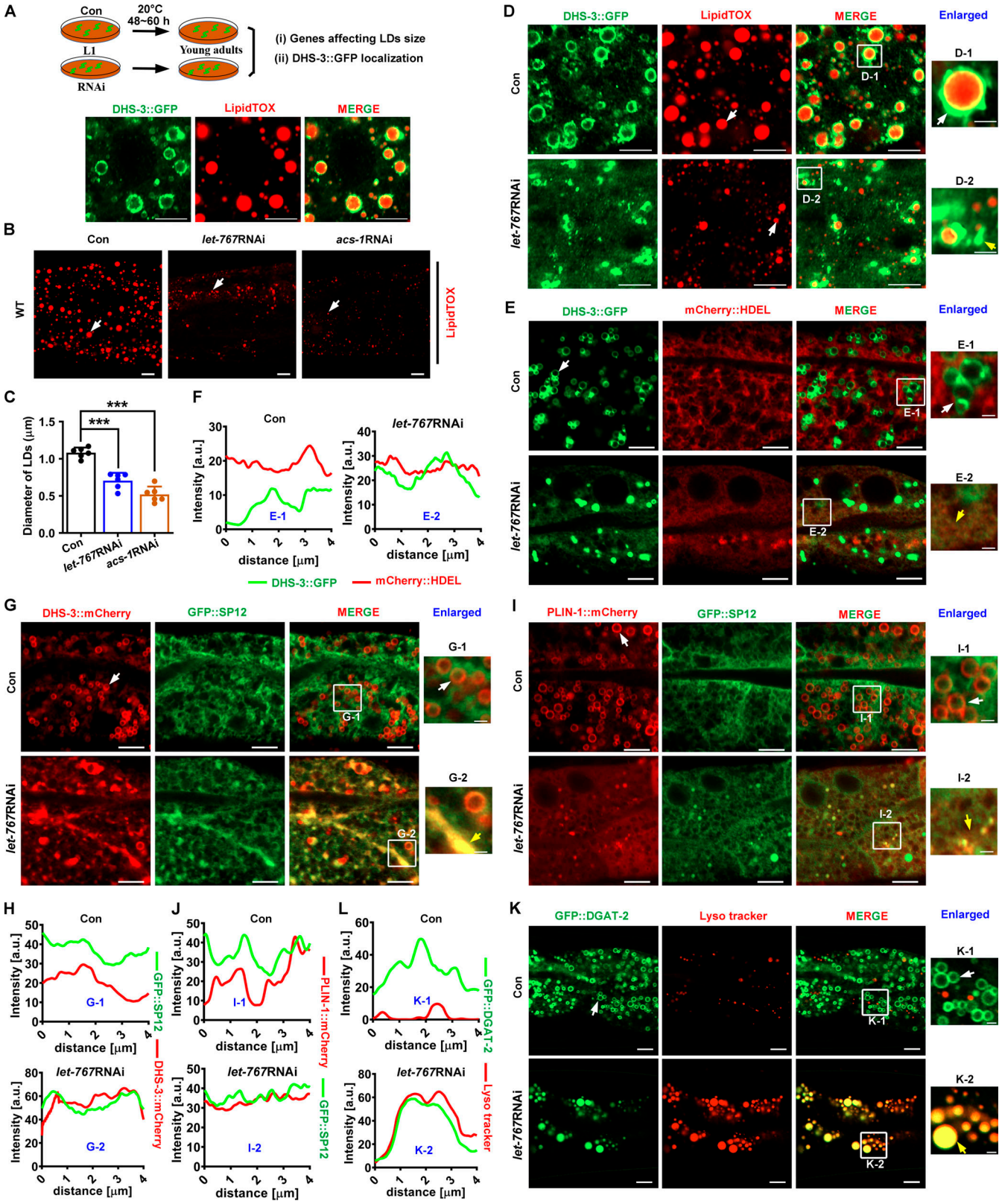

Figure 1. **Reduction of LET-767 disrupted LD protein targeting. (A)** Schematic workflow of RNAi screen for genes affecting LD size and DHS-3::GFP LD localization. LipidTOX staining of fixed worms. **(B)** LipidTOX staining of LDs in young adult WT worms under RNAi treatments. White arrows indicate LDs. **(C)** Quantification of LD diameter from B. Data are presented as mean ± SD of six representative animals for each worm strain. Statistical difference between Con and a specific RNAi treatment, ***P < 0.001 by one-way ANOVA. **(D)** Localization of DHS-3::GFP with respect to LDs stained by LipidTOX. White arrows and yellow arrows indicate the localization of DHS-3::GFP on LDs or not, respectively. The enlarged image was from the corresponding merged image. **(E)** Localization of DHS-3::GFP with respect to the ER marked by mCherry::HDEL. White arrows indicate LDs and yellow arrows indicate the localization of

DHS-3::GFP on the ER. **(F)** Intensity profiles of labeled scans from high-magnification regions, E-1 and E-2, show the localization of DHS-3::GFP visualized in E. **(G)** Localization of DHS-3::mCherry with respect to ER marked by GFP::SP12. White arrows indicate LDs and yellow arrows indicate the localization of DHS-3::mCherry on the ER. **(H)** Intensity profiles of labeled scans from high-magnification regions, G-1 and G-2, show the localization of DHS-3::mCherry found in G. **(I)** Localization of PLIN-1::mCherry with respect to ER marked by GFP::SP12. White arrows indicate LDs and yellow arrows indicate the localization of PLIN-1::mCherry on the ER. **(J)** Intensity profiles of labeled scans from high-magnification regions, I-1 and I-2, show the localization of PLIN-1::mCherry found in I. **(K)** Localization of GFP::DGAT-2 with respect to lysosome stained by Lyso tracker. White arrows indicate LDs and yellow arrows indicate the localization of GFP::DGAT-2 on the lysosome. **(L)** Intensity profiles of labeled scans from high-magnification regions, K-1 and K-2, show the localization of GFP::DGAT-2 found in K. All fluorescence images were captured by high-resolution laser confocal microscopy (ZEISS, Carl LSM800). For all of the represented animals, the anterior is on the left and the posterior is on the right. Scale bar represents 1 µm in enlarged panels and 5 µm in others, respectively, unless specifically indicated.

767(*gk553841*) worms, respectively, and found that the fluorescence of DHS-3::GFP, DHS-3::mCherry, and PLIN-1::mCherry was mostly expressed in the ER, and GFP::DGAT-2 was in the lysosome in *let-767*(*gk553841*) worms (Fig. 2, D–J). These results were completely consistent with the effects of *let-767*RNAi (Fig. 1). Thus, these results confirm that dysfunction of LET-767 either by RNAi or by gene mutation caused an altered localization of LD proteins.

LET-767 is localized to the ER and LDs

LET-767 was reported to share homology with human types 3 and 12 17β-HSD (17β-HSD3/12) (Desnoyers et al., 2007). Sequence analysis revealed that LET-767 may contain three distinct regions including a transmembrane region (1–38 amino acid [AA]), KR (NAD^+ binding site, 39–68 AA), and Adh Short (short-chain dehydrogenase, 69–316 AA) regions (Fig. 3 A). To trace the expression of LET-767, we generated a single-copy integrated strain for the translational expression of *let-767::gfp* (Fig. 3 A and Table S1). The green fluorescence of LET-767::GFP was observed mainly in the intestine and hypodermis (Fig. S1 F), the major sites for lipid synthesis and storage (Watts and Ristow, 2017). Compared with the Con, RNAi knockdown of *let-767* reduced the mRNA level of *let-767* detected by quantitative PCR (qPCR), as well as LET-767::GFP fluorescence and protein level detected with anti-GFP antibody, but not the GFP-tagged translocation-associated membrane protein 1 (GFP::TRAM-1) (Table S1) used as a Con (Fig. S1, G–I). Similarly, *tram-1*RNAi significantly and specifically reduced the green fluorescence of GFP::TRAM-1, but not LET-767::GFP (Fig. S1 G), showing the specificity and efficiency of the RNAi silencing.

As mentioned above, LET-767 protein contains three regions (Fig. 3 A). To examine which region is required for its proper location and function, we also generated two additional worm strains with truncated LET-767::GFP, which were LET-767(1-38)::GFP and LET-767(39-316)::GFP (Fig. 3 A and Table S1). The green fluorescence of LET-767::GFP was diffuse and localized to LipidTOX-stained LDs (Fig. 3 B). However, it did not display the typical ring pattern of LD proteins like DHS-3::GFP (Zhang et al., 2012), PLIN-1::mCherry, and GFP::DGAT-2 (Fig. 1). To confirm the LD location of LET-767, we isolated LDs from the *let-767::gfp; dhs-3::mcherry* worms. Confocal microscopy showed that LET-767::GFP was indeed localized to DHS-3::mCherry and Lipid Blue labeled LDs as puncta (Fig. 3 C). Moreover, western blot analysis with anti-GFP antibody also verified that LET-767 was expressed in the LD fraction but was also present with high abundance in other cellular components, including cytosol (Cyto), total membrane, and post nuclear supernatant (PNS) (Fig. 3 D). Taken together, these lines of evidence clearly support that LET-767 is localized to LDs.

Next, to examine which region in LET-767 determines its ER and LD location, we crossed *let::767::gfp*, *let-767*(*1-38*)*::gfp*, and *let-767*(*39-316*)*::gfp* into *dhs-3::mcherry* and also mCherry::HDEL worm strains (Table S1), respectively, and found that the green fluorescence of LET-767::GFP and LET-767(1-38)::GFP, but not the LET-767(39-316)::GFP, perfectly overlapped with mCherry::HDEL (the ER marker) (Fig. 3, E and F), suggesting that the N-terminal 1–38 AA of LET-767 are necessary for its location in the ER. Meanwhile, this region (1–38 AA) was also required for its localization to LDs since both LET-767::GFP and LET-767(1-38)::GFP displayed contact with DHS-3::mCherry (Fig. 3 G) or LipidTOX (Fig. 3 H) -labeled LDs, while this contact was reduced with LET-767(39-316)::GFP, which appeared somewhat diffused. Taken together, these results suggest that the transmembrane region (1–38 AA) of LET-767 is necessary for its location in both the ER and LDs.

More importantly, LET-767::GFP overexpression could completely rescue the LD size and TAG content in *let-767*(*gk553841*) worms, although it had no effect in wild-type (WT) worms (Fig. 3, I–K), suggesting that LET-767 indeed plays a role in regulating LD size and lipid homeostasis. In contrast, both *let-767*(*1-38*)*::gfp* and *let-767*(*39-316*)*::gfp* could not rescue the LD size in *let-767*(*gk553841*) worms (Fig. 3, I–K). Thus, these results suggest that the entire LET-767 protein determines its role in the regulation of LD size and lipid homeostasis.

Displacement of LD proteins by LET-767 reduction may not be due to the deficiency of C17iso and C18:1(n-9)

In *C. elegans*, LET-767 was reported to be required for the production of branched-chain and long-chain fatty acids (Fig. S2 A) (Entchev et al., 2008). Indeed, both *let-767*RNAi worms and *let-767*(*gk553841*) worms showed reduced levels of the monomethyl branched-chain fatty acids C15iso and C17iso and monounsaturated fatty acid C18:1(n-9), as well as the stearoyl-CoA desaturase (SCD) activity as indicated by the ratio of C18:1(n-9) to C18:0 (Fig. S2, B and C) to different extents. In *C. elegans*, FAT-5, FAT-6, and FAT-7 are three SCDs converting C16:0 to C16:1(n-7) and C18:0 to C18:1(n-9), respectively (Brock et al., 2006, 2007), which are substrates for biosynthesis of polyunsaturated fatty acids and also complex lipids such as TAGs, PL, and sphingolipids (Fig. S2 A). Consistently, the expression of FAT-6::GFP and FAT-7::GFP was significantly reduced in *let-767*RNAi worms compared with the Con worms (Fig. S2, D and E). Thus, these observations raised the question of whether the dislocation of LD proteins by LET-767 deficiency was due to the reduction of the branched-chain and long-chain fatty acids.

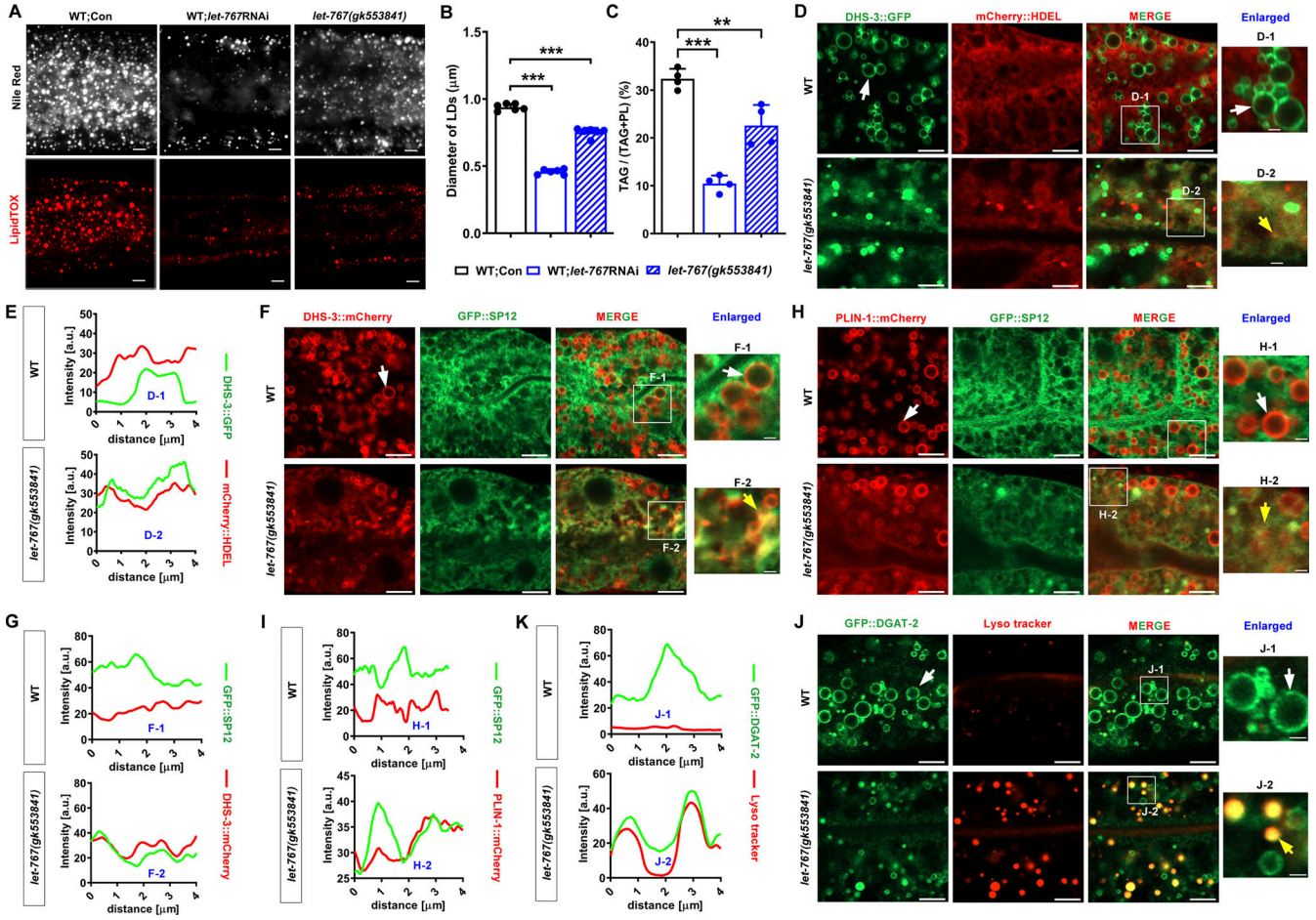

Figure 2. **Genetic mutation of *let-767* consistently led to the dislocation of LD proteins. (A)** Nile Red staining (taken by ZEISS Axio Imager M2 microscopy) and LipidTOX staining (taken by high-resolution laser confocal microscopy, ZEISS, Carl LSM800) of LDs in fixed worms. The stained particles are LDs in representative worms. **(B)** Quantification of LD diameter from A. Data are presented as the mean ± SD of six representative animals for each worm strain. **(C)** Lipid contents were measured by TLC and GC and presented as % of TAG in total lipids (TAG+PL). Data are presented as the mean ± SD of four biological repeats for each worm strain. **(D)** Localization of DHS-3::GFP with respect to ER marked by mCherry::HDEL. White arrows indicate LDs and yellow arrows indicate the localization of DHS-3::GFP on the ER. **(E)** Intensity profiles of labeled scans from high-magnification regions, D-1 and D-2, show the localization of DHS-3::GFP found in D. **(F)** Localization of DHS-3::mCherry with respect to ER marked by GFP::SP12. White arrows indicate LDs and yellow arrows indicate the localization of DHS-3::mCherry on the ER. **(G)** Intensity profiles of labeled scans from high-magnification regions, F-1 and F-2, show the localization of DHS-3::mCherry found in F. **(H)** Localization of PLIN-1::mCherry with respect to ER marked by GFP::SP12. White arrows indicate LDs and yellow arrows indicate the localization of PLIN-1::mCherry on the ER. **(I)** Intensity profiles of labeled scans from high-magnification regions, H-1 and H-2, show the localization of PLIN-1::mCherry found in H. **(J)** Localization of GFP::DGAT-2 with respect to lysosome stained by Lyso tracker. White arrows indicate LDs and yellow arrows indicate the localization of GFP::DGAT-2 on lysosome. **(K)** Intensity profiles of labeled scans from high-magnification regions, J-1 and J-2, show the localization of GFP::DGAT-2 found in J. **(D–J)** All worms were fed with *E. coli OP50*. Significant difference between WT and a specific mutant strain treated with Con or *let-767*RNAi, **P < 0.01, ***P < 0.001 by one-way ANOVA. All fluorescence images were captured by high-resolution laser confocal microscopy (ZEISS, Carl LSM800), unless specifically indicated. For all of the represented animals, the anterior is on the left, and the posterior is on the right. Scale bar represents 1 μm in enlarged panels and 5 μm in others, respectively, unless specifically indicated.

For use as positive Con, dietary supplementation of C17iso or C18:1(n-9) could completely recover the LD size and lipid accumulation indicated by GFP::DGAT-2 as well as the LipidTOX staining in *fat-6*RNAi worms and *acs-1*RNAi worms (Fig. S2, F and G), respectively, in which ACS-1 is involved in the biosynthesis of C17iso (Fig. S2 A), as we previously reported (Zhang et al., 2021). However, dietary supplementation of C17iso or C18:1(n-9) as well as the combination of C17iso and C18:1(n-9) had no effect on the lysosome misplacement of GFP::DGAT-2 in *let-767*RNAi worms (Fig. 4 A). Furthermore, the reduced LD size and lipid accumulation indicated by LipidTOX staining in both *let-767*RNAi and *let-767*(*gk553841*) worms could not be rescued by dietary supplementation of these fatty acids (Fig. 4, B and C). In *C. elegans*, dysfunction of LET-767 was shown to affect growth (Kuervers et al., 2003) and lumen formation (Zhang et al., 2011). Consistent with these reports, LET-767 reduction resulted in serious developmental delay and altered ER morphology, and these phenotypes also could not be recovered by feeding the above-mentioned dietary fatty acids (Fig. 4, D and E). Taken together, these results suggest that the displacement of LD proteins by LET-767 reduction may not be due to the lack of branched-chain and long-chain fatty acids.

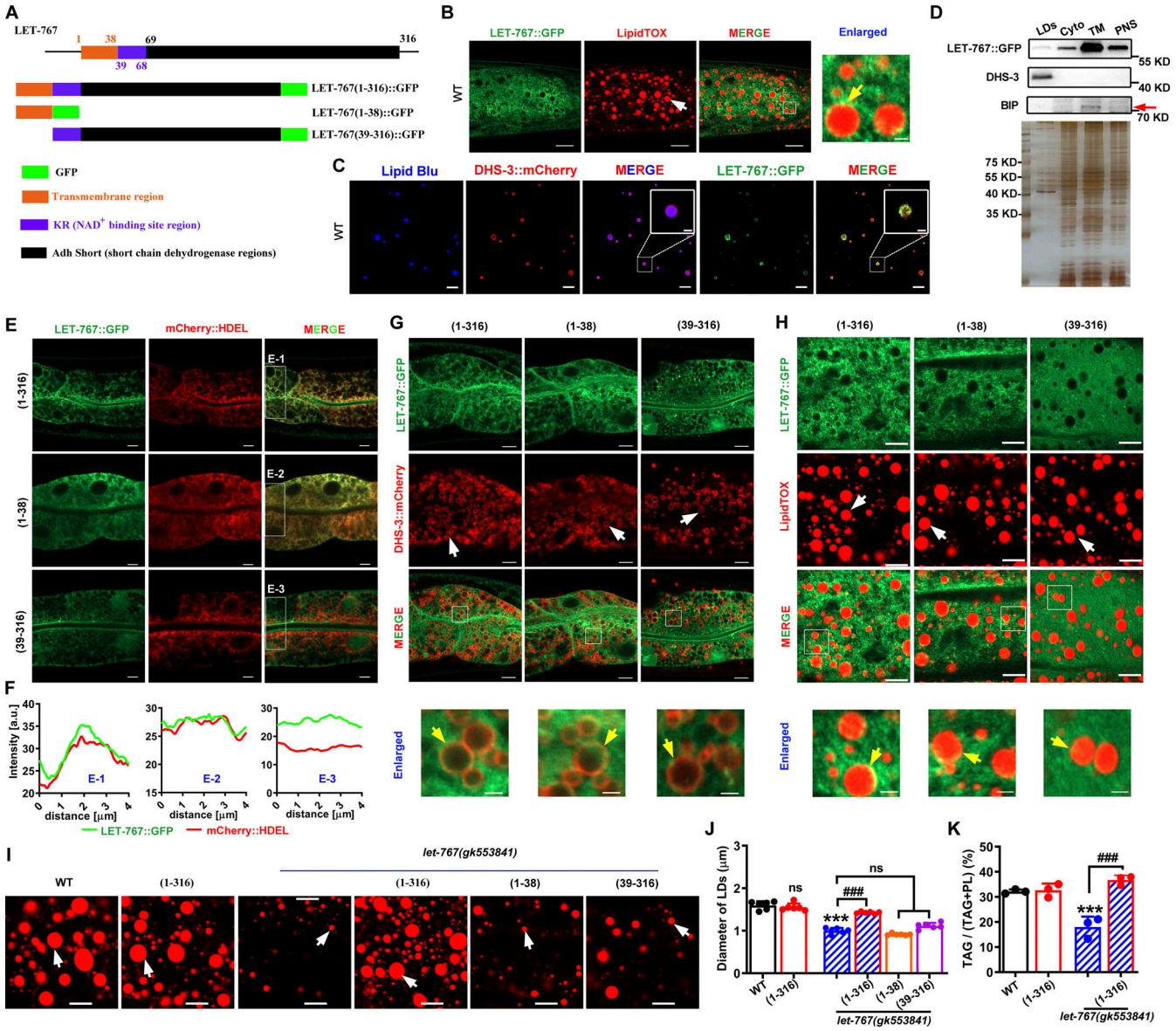

Figure 3. **LET-767 is localized in the ER and LDs. (A)** The prediction of LET-767 domain structure and schematic diagram of LET-767 truncation in *C. elegans*. Black box: Adh Short (short-chain dehydrogenase regions); blue box: KR (NAD^+ binding site regions); orange red box: transmembrane region. **(B)** Localization of LET-767::GFP on LipidTOX-stained LDs. White arrow indicates LDs and yellow arrow indicates the localization of LET-767::GFP on LDs. Scale bar in merged and enlarged panels represent 10 and 1 μm, respectively. **(C)** The localization of LET-767::GFP and DHS-3::mCherry on isolated LDs stained by Lipid Blu. **(D)** Western blot analysis of LET-767 in various cellular fractions. LET-767::GFP and DHS-3 were detected by anti-GFP antibody and anti-DHS-3 antibody, respectively. Anti-BIP antibody was employed to detect the ER, and red arrow indicates BIP (binding immunoglobulin protein). Total loading amounts were adjusted and normalized via SDS-PAGE silver staining (bottom panel). TM, total membrane. **(E)** Localization of mCherry::HDEL with various LET-767::GFP truncations. **(F)** Intensity profiles of labeled scans from high-magnification regions, E-1, E-2, and E-3, show the colocalization of LET-767::GFP and mCherry::HDEL found in E. **(G)** Localization of DHS-3::mCherry with various LET-767::GFP truncation. White arrows indicate LDs and yellow arrows indicate the overlapped LET-767::GFP with DHS-3::mCherry. **(H)** Localization of various LET-767::GFP truncations on LDs stained by LipidTOX. White arrows indicate LDs and yellow arrows indicate the localization of LET-767::GFP on LDs. **(I)** LipidTOX staining of LDs in indicated worm strains. White arrows indicate LDs. **(J)** Quantification of LD diameter from I. Data are presented as the mean ± SD of six representative animals for each worm strain. **(K)** Lipid contents were measured by TLC/GC and presented as % TAG in total lipids (TAG+PL). Data are presented as the mean ± SD of three biological repeats for each worm strain. Significant difference between WT and an indicated worm strain, ***$P < 0.001$, significant difference between two indicated worm strains, ###$P < 0.001$, the P values are indicated by one-way ANOVA. ns, no significance. All fluorescence images were captured by high-resolution laser confocal microscopy (ZEISS, Carl LSM800). For all of the represented animals, the anterior is on the left and the posterior is on the right. Scale bar represents 1 μm in enlarged panels and 5 μm in others, respectively, unless specifically indicated. Source data are available for this figure: SourceData F3.

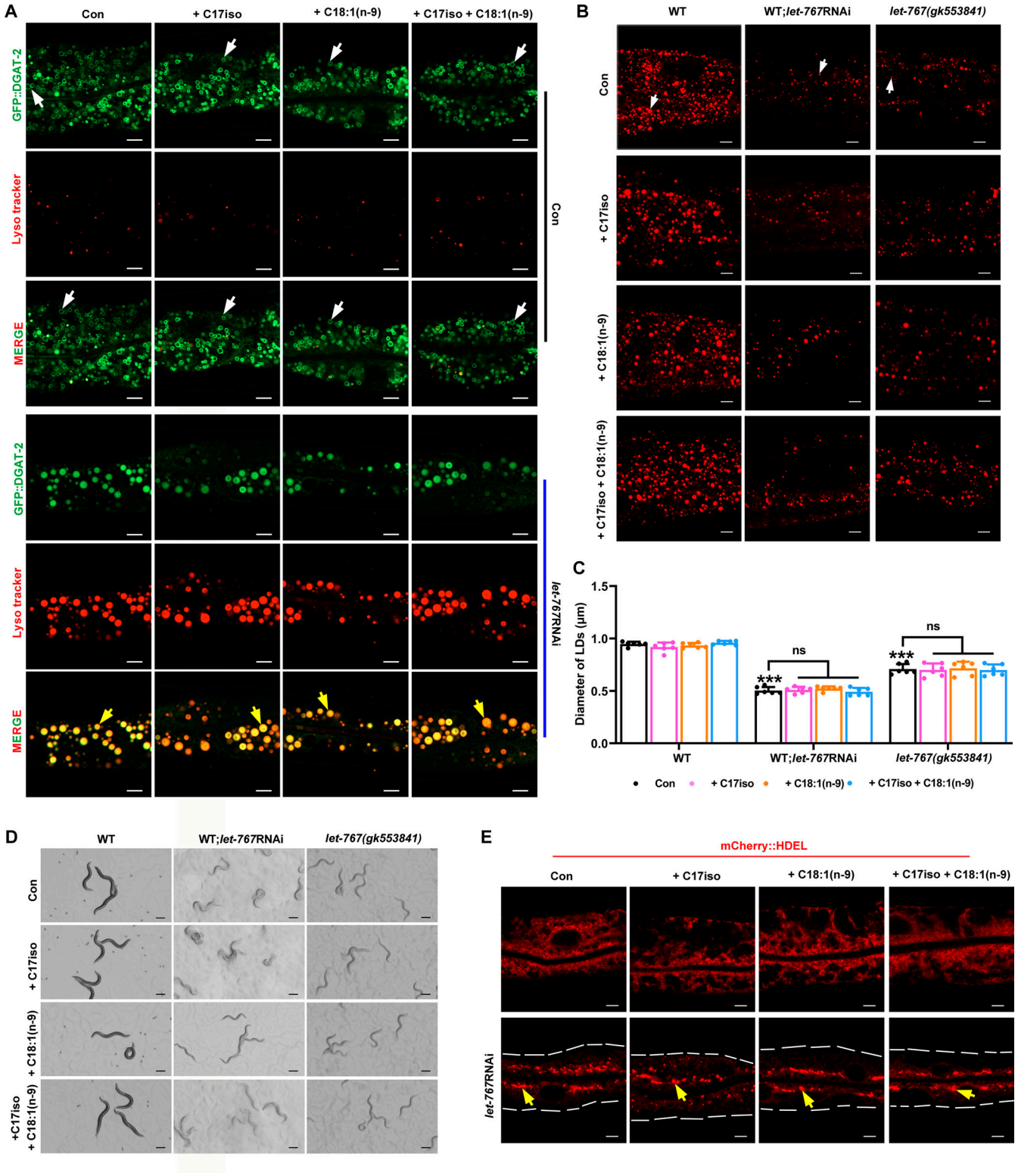

Figure 4. **Dietary supplementation of C17iso and/or C18:1(n-9) had no effects on *let-767* deficiency worms. (A)** Localization of GFP::DGAT-2 in Con and *let-767*RNAi worms supplemented with C17iso and/or C18:1(n-9). White arrows indicate LDs and yellow arrows indicate the localization of GFP::DGAT-2 on lysosome. **(B)** LipidTOX staining of LDs in fixed worms. White arrows indicate LDs. **(C)** Quantification of LD diameter from B. Data are presented as the mean ± SD of six representative animals for each worm strain. Significant difference between WT and an indicated worm strain, ***P < 0.001 by one way ANOVA; ns, no significance. **(D)** The growth and development analysis of *let-767*RNAi or *let-767*(*gk553841*) worms supplemented with C17iso and/or C18:1(n-9) at 72 h. Scale bar represents 5 mm. **(E)** Representative images of ER morphology indicated by mCherry::HDEL in *let-767*RNAi worms under treatment of dietary C17iso and/or C18:1(n-9). Yellow arrows indicate the aggregation of the ER. The white dashed lines indicate the worm boundaries. All fluorescence images were captured by high-resolution laser confocal microscopy (ZEISS, Carl LSM800). For all of the represented animals, the anterior is on the left and the posterior is on the right. Scale bar represents 5 μm, unless specifically indicated.

In addition, LET-767 was recently shown as a 3-ketoacyl reductase involved in fatty acid elongation pathway and the ER membrane quality (Garcia et al., 2023). We found that RNAi knockdown of several other genes including *sbp-1* (sterol regulatory element binding protein), *hpo-8* (enoyl-CoA hydratase), *elo-5* (3-ketoacyl synthase), *pod-2* (acetyl-CoA carboxylase), and *rab-5* (GTPase) involving in fatty acid metabolism pathway and the ER homeostasis, indeed caused an altered ER morphology indicated by mCherry::HDEL (Fig. S2 H), which was similar to *let-767*RNAi (Fig. 4 E). However, none of them affected the LD localization of DHS-3::GFP and GFP::DGAT-2 (Fig. S2, I and J), suggesting that a defect of the ER may not cause the misregulated pattern of LD proteins and LET-767 may play distinct roles in regulating the ER integrity and LD protein targeting.

LDs are wrapped by a PL monolayer. Altered LD PLs may change the tension of the LD surface, thereby affecting the location or dislocation of some LD proteins. Branched-chain and long-chain fatty acids are critical substrates for biosynthesis of PL. Inhibition of SCD/FAT-6 or ACS-1 disrupts the biosynthesis of these lipids (Brock et al., 2007; Zhang et al., 2021). However, although RNAi knockdown of either *acs-1* or *fat-6* led to small LDs as we previously reported (Zhang et al., 2021), neither knockdown affected the LD localization of DHS-3::GFP and GFP::DGAT-2 (Fig. S2, K–P). Thus, these results further demonstrate that it is the LET-767 protein itself, not altered fatty acids, that determines the LD location of these LD proteins.

LET-767 antagonizes ATGL-1 to maintain lipid homeostasis for LD protein targeting

To explore how LET-767 affected LD protein targeting and lipid accumulation, we performed an RNA sequencing (RNA-Seq) analysis between the Con worms and *let-767*RNAi worms. Differentially expressed genes were enriched into pathways such as lipid metabolism, intracellular transport, lysosome, and so on (Table S3 and Fig. 5, A and B). As mentioned above, both the SCD activity and the expression of FAT-6::GFP and FAT-7::GFP were reduced in *let-767*RNAi worms (Fig. S2, D and E). Consistently, RNA-Seq results and qPCR confirmed that the mRNA expression of *fat-6* and *fat-7* was decreased in *let-767*RNAi worms (Fig. 5, B and C). In contrast, the mRNA expression of genes involved in COPI-dependent traffic, vesicle-mediated transport, autophagy, lysosome, and lipolysis (fatty acid degradation and β-oxidation) was upregulated in *let-767*RNAi worms compared with the Con (Fig. 5, A, B, and D). These observations raised the question of whether the dislocation of LD protein and reduced LD size under LET-767 deficiency was due to the upregulation of the above pathways, instead of downregulated lipogenesis.

Both lipophagy and lipolysis play critical roles in LD degradation (Schott et al., 2019). As mentioned above, we observed that RNAi reduction (Fig. 1 K) or genetic mutation (Fig. 2 J) of *let-767* led to increased lysosome size and number by Lyso tracker staining. We further confirmed this phenomenon via another lysosome marker LMP-1::mCherry (Table S1), which colocalized with GFP::DGAT-2 under *let-767*RNAi treatment (Fig. S3 A), suggesting that DGAT-2 was indeed misplaced to the lysosome under this condition. Bafilomycin A1 is widely used to block autophagosome–lysosome fusion and to inhibit lysosome function (Mauvezin and Neufeld, 2015). Although application of Bafilomycin A1 reduced the sizes and numbers of lysosomes indicated by LMP-1::GFP (Table S1 and Fig. S3 B) and Lyso tracker (Fig. S3 C) in *let-767*RNAi worms, it could not reverse the location of GFP::DGAT-2 back to LDs (Fig. S3 C) or recover the LD size (Fig. S3 D) in these worms. Therefore, these results suggest that upregulated lysosome function may not contribute to LET-767 deficiency–triggered LD protein displacement and LD size reduction.

Next, we turned to examining the lipolysis pathway. *atgl-1* encodes an ortholog of mammalian adipose triglyceride lipase, and its expression was significantly increased in *let-767*RNAi worms compared with the Con worms (Fig. 5, B and D). Moreover, the mRNA expression of *atgl-1* was also upregulated in *let-767*(*gk552841*) worms (Fig. 5 E). Consistently, RNAi knockdown of *let-767* significantly increased the fluorescence intensity and protein level of ATGL-1::GFP (Table S1 and Fig. 5, F and G). More importantly, *let-767*RNAi treatment apparently led to translocation of ATGL-1::GFP to LDs (Fig. 5, H and I). On the other hand, RNAi knockdown of *atgl-1* significantly repressed the fluorescence intensity of ATGL-1::GFP and *atgl-l* mRNA (Fig. S3, E and F), but had no effect on the fluorescence intensity, protein level, and LD location of LET-767::GFP (Fig. S3, G–I). Taken together, these results suggest an antagonistic role of LET-767 for the expression and LD translocation of ATGL-1.

Next, we hypothesized that inhibition of activated lipolysis might rescue the decreased LD size and lipid accumulation caused by LET-767 deficiency. A previous report showed that LID-1 (LD protein 1) binds to ATGL-1 to modulate lipolysis during nutritional deprivation (Lee et al., 2014). The mRNA expression of *lid-1* was also significantly increased in *let-767*RNAi worms (Fig. 5, B and D), similar to *atgl-1* but to a lesser extent. However, inactivation of LID-1 by RNAi or gene mutation (*xd288*) had no effect on the LD size and lipid accumulation in *let-767*RNAi worms (Fig. S3, J and K). In contrast, inactivation of ATGL-1 by either RNAi or gene mutation (*xd314*) significantly increased the LD size and lipid accumulation in both *let-767*RNAi and *let-767*(*gk553841*) worms (Fig. 5, J and K). Remarkably, *atgl-1*RNAi treatment could relocate DHS-3::GFP from the ER and GFP::DGAT-2 from the lysosome back to LDs in the *let-767*RNAi worms (Fig. 5, L–N). Taken together, these results suggest that LET-767 actually antagonizes ATGL-1 to maintain lipid homeostasis for LD protein targeting.

LET-767 interacts with ARF-1 for LD protein targeting

Given the observation that LET-767 deficiency–caused LD translocation of ATGL-1 and inhibition of *atgl-1* could reverse the displacement of LD protein targeting, we thus investigated the underlying mechanism. We conducted an immunoprecipitation-mass spectrometry (IP-MS) analysis using LET-767::GFP as bait to identify its interacting proteins (Fig. S4 A). In total, 96 proteins including LET-767 were pulled down (Table S4). As well-known LD proteins, DHS-3, PLIN-1, and DGAT-2 were not detected in the IP-MS of LET-767 (Table S4). One protein of interest we noticed from our data is ARF-1 (Fig. S4 B), an ortholog of human ARF1/COPI involved in vesicular trafficking. Previous reports in other organisms or systems have shown that

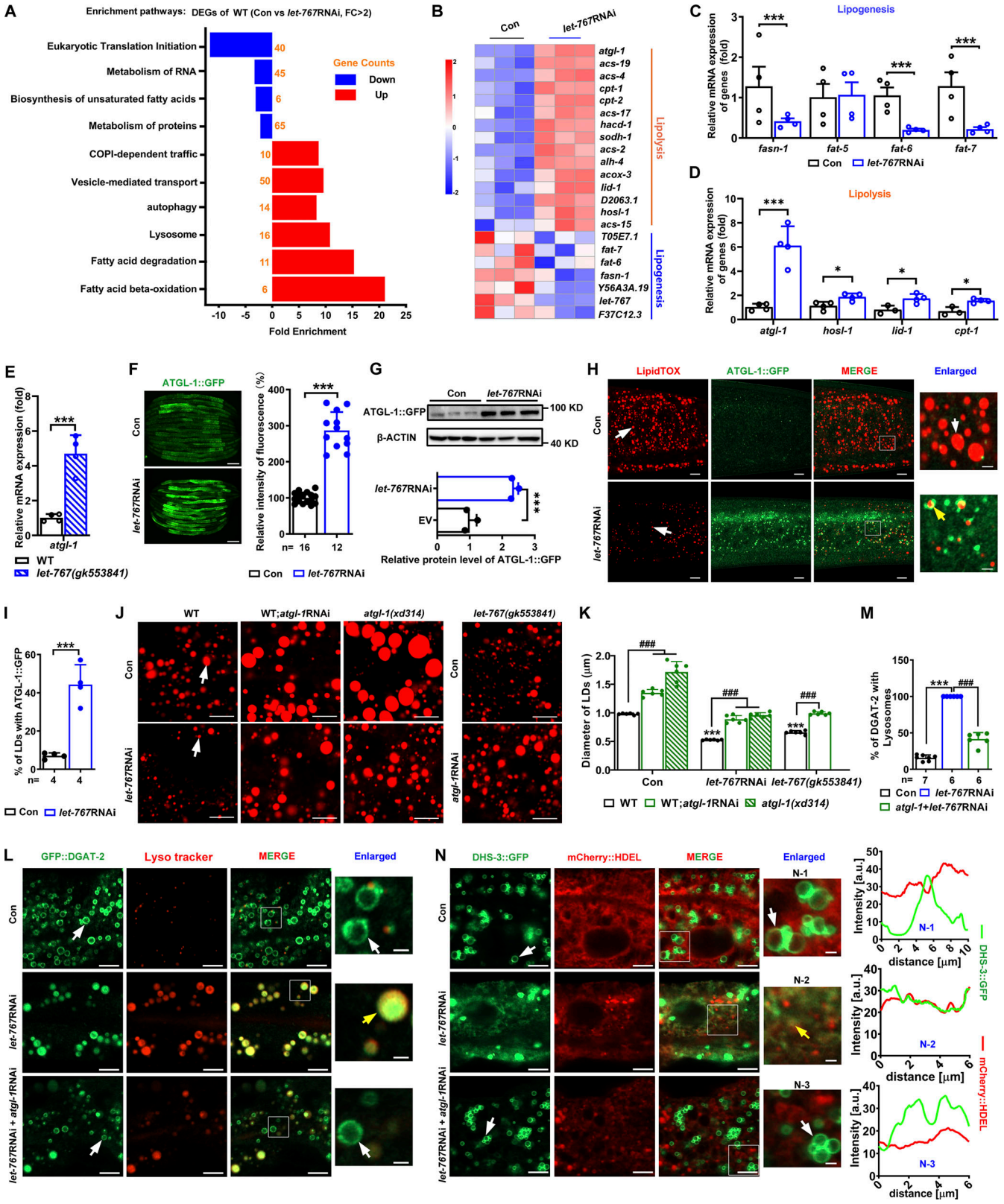

Figure 5. **LET-767 antagonizes ATGL-1 to regulate LD protein targeting and lipid homeostasis. (A)** Kyoto Encyclopedia of Genes and Genomes pathway enrichment analysis of WT worms treated with Con and *let-767*RNAi. The data was analyzed by DAVID v6.8. Blue columns indicate downregulation, and the red columns indicate upregulation. DEG, differentially expressed genes. **(B)** Heat map of lipogenesis genes and lipolysis genes from A. **(C and D)** Relative mRNA level of selected lipogenesis genes (C) and lipolysis genes (D). Data are presented as the mean ± SD of four biological repeats for each worm strain. Significant difference between Con and *let-767*RNAi, *P < 0.5, ***P < 0.001 by two-tailed *t* test. **(E)** Relative mRNA level of *atgl-1* in *let-767*(*gk553841*) mutant worm. Data are presented as the mean ± SD of four biological repeats for each worm strain. Significant difference between WT and *let-767*(*gk553841*) worms, ***P < 0.001

by two-tailed *t* test. **(F)** Fluorescence intensity (left) and quantification (right) of ATGL-1::GFP. Scale bar represents 100 µm. Images were taken by ZEISS Axio Imager M2. **(G)** Top: Western blot analysis of ATGL-1::GFP using anti-GFP antibody. Bottom: Quantification of ATGL-1::GFP. Data were normalized to the internal Con β-ACTIN. Data are presented as the mean ± SD of three biological repeats for each worm strain. Significant difference between Con and *let-767*RNAi, ***P < 0.001 by two-tailed *t* test. **(H)** Localization of ATGL-1::GFP with respect to LDs stained by LipidTOX. White arrows indicate LD and yellow arrows indicate the localization of ATGL-1::GFP on LDs. **(I)** Quantification of ATGL-1::GFP LD localization from H. **(F and I)** Statistical difference between Con and *let-767*RNAi, ***P < 0.001 by two-tailed *t* test. **(J)** LipidTOX staining of LDs in fixed worms. White arrows indicate LDs. **(K)** Quantification of LD diameter from J. Data are presented as mean ± SD of six representative animals for each worm strain. **(L)** Localization of GFP::DGAT-2 with respect to lysosome stained by Lyso tracker. White arrows indicate LDs and yellow arrows indicate the localization of GFP::DGAT-2 on lysosome. **(M)** Quantification of GFP::DGAT-2 LD localization from L. **(K and M)** Significant difference between WT and an indicated worm strain, ***P < 0.001, significant difference between two indicated worm strains, ###P < 0.001, the P values are indicated by one-way ANOVA. **(N)** Left: Localization of DHS-3::GFP with respect to ER marked by mCherry::HDEL. White arrows indicate LDs and yellow arrows indicate the localization of DHS-3::GFP on ER. Right: Intensity profiles of labeled scans from high-magnification regions, N-1, N-2 and N-3, show the localization of DHS-3::mCherry found in left. *n*, the number of measured worms for each worm strain. All fluorescence images were captured by high-resolution laser confocal microscopy (ZEISS, Carl LSM800), except F. For all of the represented animals, the anterior is on the left and the posterior is on the right. The scale bar represents 1 µm in enlarged panels and 5 µm in others, respectively, unless specifically indicated. Source data are available for this figure: SourceData F5.

Arf1/COPI proteins localize to cellular LDs, are sufficient to bud nano-LDs from cellular LDs, and are required for LD localization of specific TAG-storage and catabolism enzymes, such as ATGL, GPAT4, and DGAT2 (Beller et al., 2008; Ellong et al., 2011; Soni et al., 2009; Wilfling et al., 2014). Our RNA-Seq results also showed that LET-767 reduction activated the expression of several genes involved in COPI-dependent traffic (Fig. 5 A and Fig. S4 C). These observations raised the question of whether Arf1/COPI, like ATGL-1, is involved in the disrupted LD protein targeting and decreased lipid accumulation caused by LET-767 reduction.

To this end, we first examined six potential Arf/COPI genes with available RNAi clones and found that RNAi knockdown of *arf-1* but not the others significantly increased the LD size of *let-767*RNAi worms (Fig. S4, D and E) and also *let-767*(*gk553841*) worms (Fig. 6, A and B). Compared with the WT (N2), deletion (*ok796*) of *arf-1* significantly restored the LD size and TAG content of *let-767*RNAi worms (Fig. 6, C–E), which displayed similar phenotypes as *atgl-1*(*xd314*) (Fig. 5, J and K; and Fig. 6 E). Next, to confirm the interaction between LET-767 and ARF-1, we generated a transgenic strain for the translational expression of ARF-1::RFP (Table S1). The red fluorescence of ARF-1::RFP was observed throughout the whole body of worms including the head, intestine, and hypodermis (Fig. S4 F). RNAi knockdown of *arf-1* significantly reduced the fluorescence of ARF-1::RFP (Fig. S4, G and H), suggesting the efficiency of the RNAi. Confocal microscopy showed that, unlike LET-767::GFP, ARF-1::RFP did not show colocalization with GFP::DGAT-2, DHS-3::GFP, and LipidTOX (green) (Fig. S4 I), suggesting that ARF-1 may not localize to LDs in *C. elegans*. In contrast, ARF-1::RFP did overlap with GFP::SP12 in the intestine (Fig. S4 J), suggesting the ER localization of ARF-1. Compared with the Con, the fluorescence level of ARF-1::RFP was significantly increased by *let-767*RNAi (Fig. S5 A). On the other hand, *arf-1*RNAi did not affect the fluorescence expression and LD location of LET-767::GFP (Fig. S5, B–D), which is similar to the relationship between LET-767 and ATGL-1 (Fig. S3, G–I).

Confocal microscopy and Co-IP analysis consistently confirmed a colocalization between LET-767::GFP and ARF-1::RFP (Fig. 6, F and G). Furthermore, we found that ARF-1 could interact with either the transmembrane region (1–38 AA) or KR+Adh region (39–316 AA) of LET-767 indicated by confocal microscopy analysis (Fig. 6 F) and Co-IP analysis (Fig. 6 G). More importantly, although RNAi knockdown of *arf-1* did not affect the LD targeting of GFP::DGAT-2 and DHS-3::GFP, it could reverse their misplacement from the lysosome and ER back to LDs, respectively, in the *let-767*RNAi background (Fig. 6, H–K). Taken together, these lines of evidence suggest that LET-767 interacts with ARF-1 to ensure appropriate LD protein targeting.

LET-767 deficiency promotes ARF-1 to recruit ATGL-1 for LD translocation

Since ARF-1 and ATGL-1 displayed similar phenomena under LET-767 deficiency, it raised the question regarding their relationship. As mentioned above, *let-767*RNAi treatment led to the LD translocation of ATGL-1::GFP (Fig. 5 H), and a similar effect was observed with ARF-1::RFP as well (Fig. 7 A), suggesting that both ARF-1 and ATGL-1 are recruited to LDs under LET-767 deficiency. Therefore, we asked whether there is a direct interaction between ARF-1 and ATGL-1. Confocal microscopy analysis revealed an obvious colocalization of ARF-1::RFP with ATGL-1::GFP under *let-767*RNAi treatment (Fig. 7 B). Meanwhile, Co-IP analysis using anti-GFP or anti-FLAG antibody consistently showed a direct interaction between ATGL-1::GFP and ARF-1::RFP, which was somewhat enhanced under *let-767*RNAi treatment (Fig. 7 C).

Next, we examined whether the increased expression and LD location of ATGL-1 were dependent on ARF-1. In the Con worms, RNAi knockdown of *arf-1* did not affect the expression of ATGL-1::GFP; however, it did alleviate the increased fluorescence and protein level of ATGL-1::GFP in *let-767*RNAi worms (Fig. 7, D and E). More importantly, the LD translocation of ATGL-1::GFP in *let-767*RNAi worms was remarkably reversed under *arf-1*RNAi treatment (Fig. 7, F and G), suggesting that LET-767 deficiency–induced expression and LD relocation of ATGL-1 are dependent on ARF-1. As Con, *fat-6*RNAi or *acs-1*RNAi, which had no effect on LD targeting of DHS-3::GFP and GFP::DGAT-2 (Fig. S2, H–M), did not affect the expression and location of ARF-1::RFP and ATGL-1::GFP, although *acs-1*RNAi slightly repressed the fluorescence intensity of ATGL-1::GFP (Fig. S5, E–H). Altogether, these lines of evidence indicate that ARF-1 interacts with ATGL-1 to facilitate their LD translocation, thereby preventing the LD targeting of LD proteins such as DHS-3, PLIN-1, and DGAT-2, when LET-767 is dysfunctional.

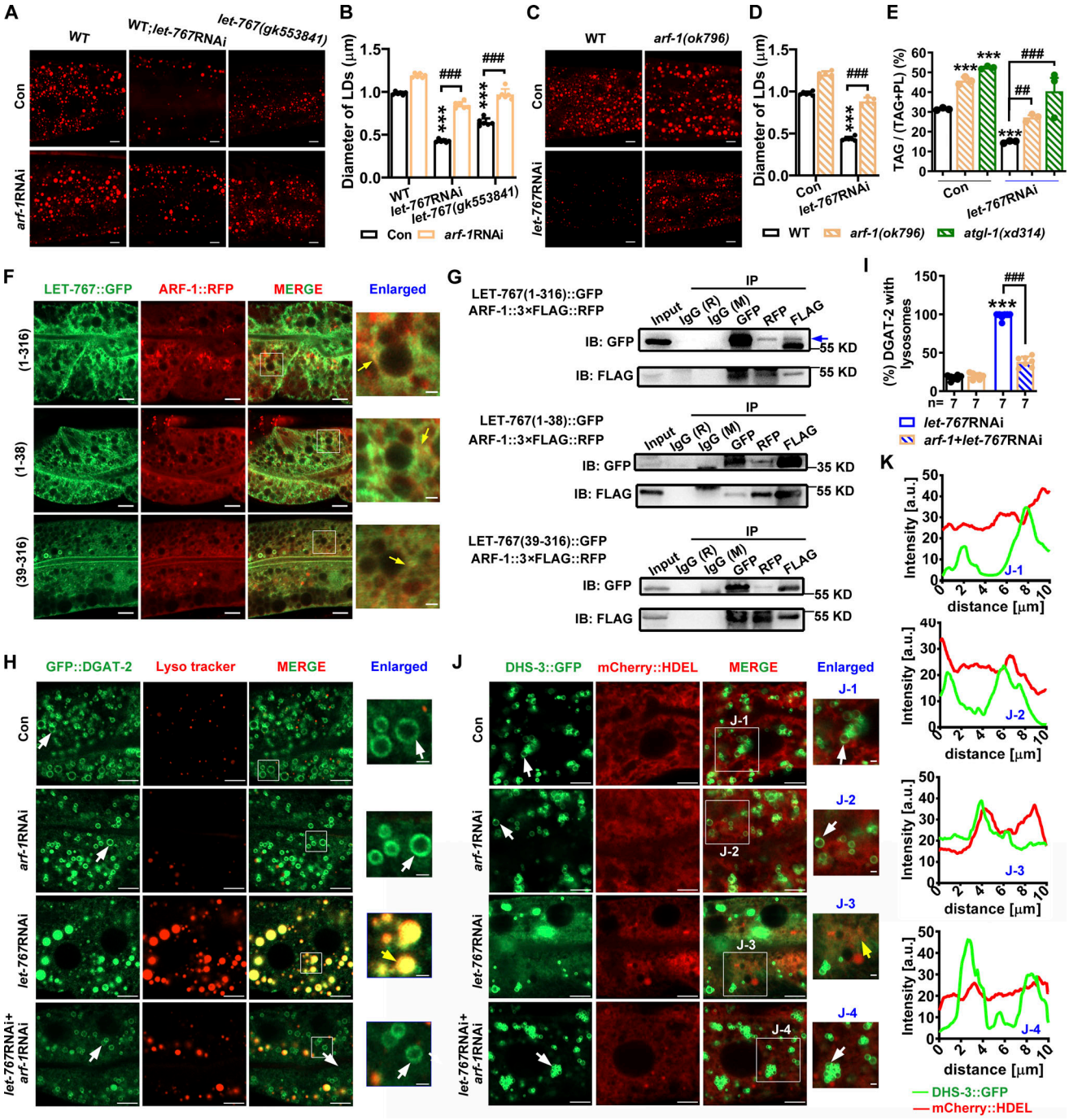

Figure 6. **LET-767 interacts with ARF-1 to ensure proper LD protein targeting. (A and C)** LipidTOX staining of LDs in fixed worms. **(B and D)** Quantification of LD diameter from A and C, respectively. Data are presented as the mean ± SD of six representative animals for each worm strain. **(E)** Lipid contents were measured by TLC/GC and presented as % TAG in total lipids (TAG+PL). Data are presented as the mean ± SD of three biological repeats for each worm strain. **(F)** Localization of ARF-1::RFP with LET-767::GFP truncations. Yellow arrows indicate the overlapped ARF-1::RFP with LET-767::GFP. **(G)** Co-IP showed that ARF-1 interacts with LET-767 truncations detected by anti-FLAG or anti-GFP antibody. IB, immunoblot. **(H)** Localization of GFP::DGAT-2 with respect to LD stained by Lyso tracker. White arrows indicate LDs and yellow arrows indicate the localization of GFP::DGAT-2 on lysosome. **(I)** Quantification of GFP::DGAT-2 LD localization from H. *n* = 7 for each worm strain and presented as the mean ± SD. **(J)** Localization of DHS-3::GFP with respect to ER marked by mCherry::HDEL. White arrows indicate LDs and yellow arrows indicate the localization of DHS-3::GFP on ER. **(K)** Quantification of DHS-3::GFP LD localization from J. Significant difference between WT and an indicated worm strain, ***P < 0.001, significant difference between two indicated worms, ###P < 0.001, the P values are indicated by one-way ANOVA. All fluorescence images were captured by high-resolution laser confocal microscopy (ZEISS, Carl LSM800). For all of the represented animals, the anterior is on the left and the posterior is on the right. Scale bar represents 1 μm in enlarged panels and 5 μm in others, respectively, unless specifically indicated. Source data are available for this figure: SourceData F6.

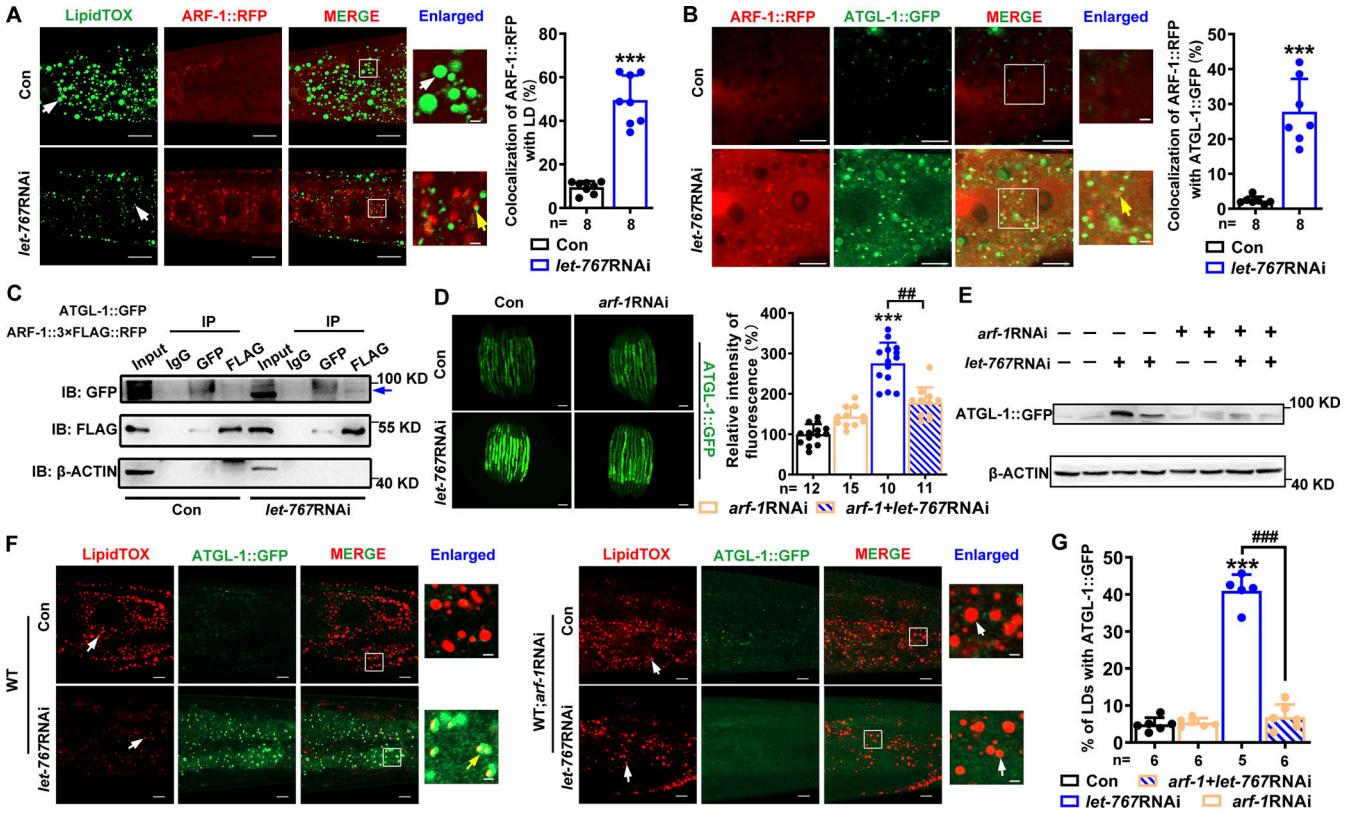

Figure 7. **ARF-1 recruits ATGL-1 for their LD translocation. (A)** Left: Localization of ARF-1::RFP with respect to LDs stained by LipidTOX (green). White arrows indicate LDs and yellow arrows indicate the localization of ARF-1::RFP on LDs. Right: Quantification of the colocalization of ARF-1::RFP with LipidTOX (green). **(B)** Left: Colocalization of ATGL-1::GFP with ARF-1::RFP, indicated by yellow arrows. Right: Quantification of the colocalization of ATGL-1::GFP and ARF-1::RFP. **(A and B)** Significant difference between Con and *let-767*RNAi, ***P < 0.001 by two-tailed *t* test. **(C)** Co-IP showed that ARF-1 directly interacts with ATGL-1 detected by anti-FLAG or anti-GFP antibody. IB, immunoblot. Blue arrow indicates the target band. **(D)** Fluorescence intensity (left) and quantification (right) of ATGL-1::GFP. Scale bar represents 100 µm. Images were taken by ZEISS Axio Imager M2. **(E)** Western blot of ATGL-1::GFP detected by anti-GFP antibody and its quantification by normalization to the internalized Con β-ACTIN. Data are presented from two biological repeats for each worm strain. **(F)** Localization of ATGL-1::GFP with respect to LDs stained by LipidTOX. White arrows indicate LDs and yellow arrows indicate the localization of ATGL-1::GFP on LDs. **(G)** Quantification of ATGL-1::GFP LD localization from F. **(D and G)** Significant difference between Con and RNAi, ***P < 0.001, significant difference between two indicated worm strains, ##P < 0.01, ###P < 0.001, the P values are indicated by one-way ANOVA. Data are presented as the mean ± SD, *n*, the number of measured worms for each worm strain. All fluorescence images were captured by high-resolution laser confocal microscopy (ZEISS, Carl LSM800), except D. For all of the represented animals, the anterior is on the left and the posterior is on the right, except A is the opposite. Scale bar represents 1 µm in enlarged panels and 5 µm in others, respectively, unless specifically indicated. Source data are available for this figure: SourceData F7.

Discussion

LDs play multiple important roles in cells. How proteins correctly target LDs is critical for maintaining LD functions. In this study, taking advantage of a candidate screen in *C. elegans*, we identified LET-767 as a novel regulator to determine LD protein targeting and lipid homeostasis. We found that LET-767 is localized in both the ER and LDs and interacts with ARF-1 to prevent ARF-1 LD translocation and recruitment of ATGL-1 to maintain appropriate LD protein targeting and lipid homeostasis. Dysfunction of LET-767 by both RNAi knockdown and gene mutation consistently disrupted the LD targeting of LD marker proteins DHS-3, PLIN-1, and DGAT-2, while reversely promoting the LD translocation of ARF-1 and ATGL-1 for lipolysis, which eventually led to reduced LD size and lipid accumulation (Fig. 8).

LET-767 is a homolog of 17β-HSD (Desnoyers et al., 2007). Limited studies have reported that LET-767 is involved in growth and development (Kuervers et al., 2003), tubulogenesis and lumen formation (Zhang et al., 2011), and recently ER stress (Garcia et al., 2023). LET-767 was present in two *C. elegans* LD proteomes (Vrablik et al., 2015; Zhang et al., 2012), but whether it is an LD protein has not yet been characterized. Our work revealed that LET-767 locates in both the ER and LDs, which is dependent on its N-terminus transmembrane region (1–38 AA). GFP fluorescence and biochemical analysis demonstrated that LET-767 is an LD protein, although it does not form typical ring like LD markers DHS-3, PLIN-1, and DGAT-2. Dysfunction of LET-767 disrupted LD protein targeting as well as reduced LD size and lipid accumulation. Thus, our work uncovers an uncharacterized role of LET-767 in LD biology.

Thus far, two major and distinct pathways, CYTOLD and ERTOLD, for proteins targeting LDs have been unraveled (Olarte et al., 2022). LET-767::GFP is not only detected in LDs but also in other intracellular fractions including colocalization with the ER markers mCherry::HEDL, suggesting that LET-767 may be a ER-to-LD protein. Deletion of the transmembrane region (1–38 AA) in LET-767 affects its ability to localize to both LDs and the ER.

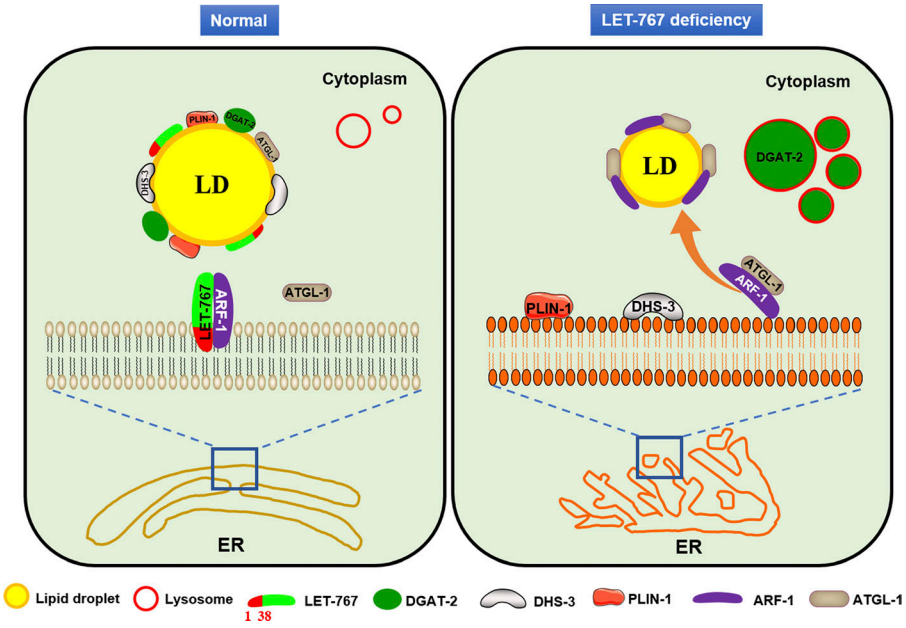

Figure 8. **A working model of LET-767 required for LD protein targeting.** Under normal condition (left panel), LET-767 presents in the ER and LDs, where it interacts with ARF-1 to prevent ARF-1 LD translocation and recruitment of ATGL-1, thereby maintaining appropriate lipid homeostasis and LD translocation of LD proteins DHS-3, PLIN-1, and DGAT-2. Under LET-767 deficiency (right panel), ARF-1 is released, and it recruits ATGL-1 to the LDs for lipolysis, which may reversely inhibit the targeting of DHS-3, PLIN-1, DGAT-2 to the LDs. LET-767 deficiency also alters ER morphology.

How LET-767 localizes in the ER and is translocated to LDs, and whether it acts like other known ER-to-LD proteins, needs further investigation. In mammalian systems, DGAT-2 (Stone et al., 2006) and ATGL (Smirnova et al., 2006) are classified into ER-TOLD pathway proteins, while perilipins (Rowe et al., 2016) are CYTOLD-targeting proteins. In *C. elegans*, DHS-3 (Zhang et al., 2012), PLIN-1 (Na et al., 2015), and DGAT-2 (Xu et al., 2012) are reported as LD proteins, though the N-terminus of DHS-3 determines its LD association (Liu et al., 2018), but how they target LDs is unknown. Deficiency of LET-767 led to the dislocation of DHS-3::GFP/DHS-3::mCherry and PLIN-1::mCherry to the ER, and GFP::DGAT-2 to the lysosome, instead of in LDs. Thus, LET-767 is necessary for appropriate LD targeting of DHS-3, PLIN-1, and DGAT-2 no matter whether they transit via the ERTOLD or CYTOLD pathway.

Vesicle-associated membrane protein-associated protein was found in a primary adipocyte LD-associated proteome (Ding et al., 2012). Arf1/COPI proteins are required for LD localization of some proteins such as ATGL, GPAT4, and DGAT2 (Beller et al., 2008; Ellong et al., 2011; Soni et al., 2009; Wilfling et al., 2014). Although deficiency of ARF-1 alone in *C. elegans* did not affect DHS-3, PLIN-1, and DGAT-2 targeting LDs, ARF-1 could recruit and interact with ATGL-1 for their LD translocation when LET-767 was dysfunctional, suggesting a conserved role of ARF-1 regulating ATGL-1 LD localization, in spite of its dependence on LET-767 deficiency. On the other hand, interestingly, inactivation of LET-767 disrupted the LD targeting of DHS-3, PLIN-1, and DGAT-2, but oppositely promoted the expression and the LD translocation of ARF-1. Moreover, inhibition of ARF-1 could reverse LET-767 deficiency caused LD displacement of DHS-3, PLIN-1, and DGAT-2. Thus, the increased expression and LD location of ARF-1 triggered by LET-767 deficiency may actually function to prevent the LD localization of DHS-3, PLIN-1, and DGAT-2, which is distinguished from the well-characterized role of Arf1/COPI for LD localization of GPAT4 and DGAT2 in other systems (Beller et al., 2008; Ellong et al., 2011; Soni et al., 2009; Wilfling et al., 2014). Therefore, Arf1/COPI may play dual roles in a context-dependent manner regulating LD protein targeting. Interestingly, a recent report also showed that either inactivated yArf1 or hyperactive yArf1 could induce LD formation and TAG accumulation (Enkler et al., 2023).

Arf1/COPI was reported to promote the formation of ER-LD membrane bridges for LD translocation of some LD proteins (Wilfling et al., 2014). However, we observed that ARF-1 is mostly expressed in the ER, but is not present in LDs under normal conditions in *C. elegans*. Moreover, deficiency of ARF-1 in *C. elegans* did not affect DHS-3, PLIN-1, and DGAT-2 targeting LDs, implying that ARF-1 may not directly be involved in the ER-LD bridge for DHS-3, PLIN-1, and DGAT-2 targeting to LDs in *C. elegans*. Given that the location of LET-767 is in both the ER and LDs, whether LET-767 plays a role in mediating the ER and LD contact or bridge for the LD translocation of LD proteins, at least for DHS-3, PLIN-1, and DGAT-2, needs to be further investigated.

Materials and methods

C. elegans strains and maintenance, RNAi

Unless specifically indicated, worms were maintained on NGM (nematode growth medium) plates seeded with *E. coli HT115*, which is the host strain for RNAi interference at 20°C. Strains were obtained from the Caenorhabditis Genetic Center or kindly provided by the Xun Huang lab (Institute of Genetics and Developmental Biology, Beijing, China), Pingsheng Liu lab (Institute of Biophysics, Beijing, China), Ho Yi Mak lab (Hong Kong University of Science and Technology, Hong Kong), Jennifer L. Watts lab, Xiaochen Wang lab (Institute of Biophysics, Beijing, China), and Chonglin Yang lab (Yunnan University, Kunming, China). Strains used in this study are listed in Table S1. For construction of transgenic worms, constructed plasmids were injected into *EG4322* (*ttTi5605*; *unc-119*[*ed9*]) following the MOS (Minos 1) protocol (Frøkjaer-Jensen et al., 2008).

Transgenic worms were constructed by homologous recombination. LET-767::GFP worms were generated by fusing *let-767p::let-767* (2.25 kb promoter and full length of *let-767*), *gfp* (amplified from pPD95.77), and linearized *pCFJ151* (amplified from *pCFJ151*, kindly provided by Shouhong Guang lab). LET-767(1-38)::GFP worms were generated by fusing *let-767p::let-767(1-38)* (2.25 kb promoter and 1–38 AA of *let-767*), *gfp*, and linearized *pCFJ151*. LET-767(39-316)::GFP worms were generated by fusing *let-767p* (2.25 kb promoter of *let-767*), *let-767(39-316)* (39–316 AA of *let-767*), *gfp*, and linearized *pCFJ151*. ARF-1::RFP worms were generated by fusing *arf-1p::arf-1, flag::rfp* (amplified from Lenti V2-FLAG-RFP) and linearized *pCFJ151*. The following primers were used for amplification of indicated fragments for homologous recombination: 5′-GGATATCTGGATCCACGAACAAGCACTGAACACCACGAGC-3′ and 5′-GTCGACCTGCAGGCATGCAACTGAGATTTGGCTTCTCTTCC-3′ (*let-767p::let-767*), 5′-GGATATCTGGATCCACGAACAAGCACTGAACACCACGAGC-3′ and 5′-GTCGACCTGCAGGCATGCAATGGCGACAGAAGAACGTA-3′ (*let-767p::let7-67*[*1-38*]), 5′-GGATATCTGGATCCACGAACAAGCACTGAACACCACGAGC-3′ and 5′-CATGTTACCTGGAATTTACAG-3′ (*let-767p*), 5′-CTGTAAATTCCAGGTAACATGGATTTGAAGAAAAGAGCTGGA-3′ and 5′-TTCTAGATGGATCTAGTGGTC-3′ (*let-767*[*39-316*]), 5′-TTGCATGCCTGCAGGTCGAC-3′ and 5′-CCAGAGCTCACCTAGGTATCTGCCGACTAGTAGGAAACAGT-3′ (*gfp*), 5′-AGATACCTAGGTGAGCTCTGG-3′ and 5′-TTCGTGGATCCAGATATCC-3′ (linearized *pCFJ151*), 5′-GGATATCTGGATCCACGAAGTCTGACGAAGAAGATGACC-3′ and 5′-CGTCATGGTCTTTGTAGTCAGATCTATTCTTGAGCTGGTTG-3′ (*arf-1p::arf-1*), and 5′-GACTACAAAGACCATGACGGTGATTATAAAGATCATGACATCGATTACAAGGATGACGATGACAAGATGGCCTCCTCCGAGGACG-3′ and 5′-TTAGGCGCCGGTGGAGTG-3′ (*flag::rfp*).

Feeding RNAi was performed using *E. coli* HT115 carrying the L4440 plasmid as empty vector Con or double-stranded RNA–expressing plasmids targeting the genes of interest. RNAi bacteria were cultured overnight at 37°C in Luria-Bertani containing 100 μg/ml ampicillin and then seeded onto the NGM plates supplemented with 100 μg/ml ampicillin and 1 mM isopropyl β-D-thiogalactopyranoside.

Nile Red and LipidTOX staining of fixed worms

Nile Red and LipidTOX (red, green) were used as the fluorescent dyes for staining of neutral lipids. Staining of fixed worms was conducted as previously described (Wu et al., 2018). Briefly, around 1,000 young adult worms (1 day old) were collected and fixed with 10% paraformaldehyde. After three freeze–thaw cycles, LDs within the worm cells were stained with 2 μl Nile Red (0.5 mg/ml, N1142; Invitrogen) or LipidTOX solution (1:4,000, H34475, H34476; Life Technologies) for 60 min at room temperature. Worms were washed three times with M9 buffer and mounted onto 2% agarose pads for microscopic observation and photography. The images were captured via the ZEISS Axio Imager M2 fluorescence microscope (Carl ZEISS) equipped with an Axiocam 506 mono camera and controlled by ZEN 3.0 software or a high-resolution laser confocal microscope (LSM800; Carl ZEISS) with a Plan-Apochromat 63×/1.4 Oil DIC (differential interference contrast microscope) objective and PMT (photomultiplier) and GaAsP detectors by identical settings unless specifically indicated, which were used to measure the diameter of the LDs in the posterior of the intestine with ZEISS3.0 lite standard software (ZEISS, Germany). Three or four biological repeats were performed. In each biological repeat, >100 individual worms were observed for phenotype determination, and six representative worms were measured for the mean diameter of LDs in each worm strain.

Bafilomycin A1 treatment and Lyso tracker staining

Synchronized L1 worms were cultured to early L4, and then the Bafilomycin A1 (CAS#: 88899-55-2; MCE) was supplemented to the plates at a final concentration 40 μM (diluent with M9 solution). After incubating at least 12 h to young adults, worms were stained for 3 h via Lyso tracker (Red DND-99, L7528; Invitrogen; LysoTracker) in the cultured plates at 1:500 dilutions (diluent with M9 solution). Finally, worms were washed two times with M9 buffer and mounted onto 2% agarose pads for microscopic observation and photography with a high-resolution laser confocal microscope (LSM800; Carl ZEISS) with a Plan-Apochromat 63×/1.4 Oil DIC objective and PMT and GaAsP detectors. Image processing was performed with ZEN software, black edition (Carl Zeiss), and the images were analyzed using ZEN 3.0 software (Carl Zeiss).

Analysis of TAG

The extraction, separation, and analysis of worm lipids were performed as described before (Wu et al., 2018). In general, about 40,000 young adult worms were harvested for total lipid extraction, the extracted lipid samples were loaded in triplicate on Thin-Layer Chromatography (TLC) Silica gel 60G 25 Glass-plates (HX16244921; Supelco), and then developed to the top of the plate in the solvent system hexane: diethyl ether: acetic acid (80:20:2). Individual TAG and PL bands were then scraped off from the TLC plates with 1 ml of MeOH + 2.5% H_2SO_4 added for methylation., Finally, fatty acids were analyzed with an Agilent 7890A gas chromatograph (GC). The content of TAG or PL was determined by counting the fatty acids from each sample and was shown as the percentage of TAG in total lipids (TAG + PL). Three or four biological replicates were performed for TLC analysis.

Analysis of fatty acid compositions

Approximately 2,000 young adults were harvested for fatty acid extraction and analysis. To extract fatty acids and form methyl esters, 1 ml of MeOH + 2.5% H_2SO_4 was added to the harvested worms. They were then heated for 2 h at 70°C. Determination of the fatty acids was done with an Agilent 7890A GC (Zhang et al., 2021). Four biological replicates were performed for GC analysis.

Dietary supplementation of fatty acids

C18:1(n-9) (CDDE-U-46-A; ANPEL) was supplemented into worm growth media plates at a final concentration 0.2 mM, and C17iso (11-1615; Larodan) was dissolved in 100% DMSO and mixed with cultured bacteria to 1 mM working concentration. The mixtures were spotted onto plates for culturing worms. Experimental and Con plates for a given assay were prepared with DMSO-supplemented bacterial food (Zhang et al., 2021).

mRNA isolation and qPCR

Synchronized young adult worms were harvested in RNAiso plus (9109; Takara), as previously described (Wu et al., 2018), after being crushed by a syringe and extracting the total RNA sequentially with chloroform and isopropanol, dissolved in diethyl pyrocarbonate–treated water. Then they were reversely transcribed to cDNA using the PrimeScript RT reagent kit (RR047A; Takara Bio, Inc.). mRNA levels were quantified in four biological replicates using SYBR Green Master Mix (Applied Biosystems) following manufacturers' standard protocol on a real-time PCR instrument 7900HT (ABI).

The following primers were used to detect the mRNAs level of indicated genes: 5′-TTTCACAAATGGGAGGAGGC-3′ and 5′-GTCCACCCCAAAGCCAATC-3′ (*tbb-2*), 5′-TCATGGATCCACAAG TTCGAC-3′ and 5′- TACAGTATCTGGGTCTTGTG-3′ (*fasn-1*), 5′-CGATTTGTACGAGGATCCGGTG-3′ and 5′- CAGTGGGAGACA CTGTTGATGC-3′ (*fat-5*), 5′-TCTACCAGCTCATCTTCGAGGC-3′ and 5′-GATCACGAGCCCATTCGATGAC-3′ (*fat-6*), 5′-GGAAGG AGACAGCATTCATTGCG-3′ and 5′-GTCTTGTGGGAATGTGTG GTGG-3′ (*fat-7*), 5′-ACGTTCTTCTGTCGCCAATCG-3′ and 5′-AGGAGCAGCGTTGGTGAAGTCG-3′ (*let-767*), 5′-CTCCATGCA TACGTTGTCTC-3′ and 5′-CCTCGAGTGGAATATCACTG-3′ (*atgl-1*), 5′-CAAAGTTTGGCGGACACAGC-3′ and 5′-CAGGGAGGCAAC TGGCAC-3′ (*hosl-1*), 5′-TGAATTGGATGACATTCACG-3′ and 5′-CTATTGCTTCGCCGTTTAGG-3′ (*lid-1*), and 5′-GATTGCCGATGT TGAGATGT-3′ and 5′-TGCTTTACGGAGGAGTTGG-3′ (*cpt-1*). The relative abundance of mRNA transcripts was determined using the ΔΔCt method and *tbb-2* was used as a reference gene.

Isolation of LDs

About 2.0 × 10^5 young adult worms were harvested in M9 buffer and washed three times with double distilled water (ddH_2O) on ice. Worms were then washed twice with buffer A (25 mM Tricine, pH 7.6, 250 mM sucrose, and 0.2 mM phenylmethylsulfonyl fluoride) and resuspended in 5 ml buffer A. The worms were homogenized by dounce with protease inhibitor cocktail (P8340; Sigma-Aldrich) and phenylmethylsulfonyl fluoride on ice. 1.5 ml of the supernatant fraction (PNS) was transferred to a 2 ml EP tube. 0.5 ml buffer B (20 mM HEPES, pH 7.4, 100 mM KCl, and 2 mM $MgCl_2$) was carefully added on top of the supernatant. The tube was then centrifuged at 10,000 *g* for 60 min at 4°C to allow the LDs to float to the top layer (Zhang et al., 2012). The LD fraction was carefully collected from the top layer of the gradient and washed with 200 µl buffer B three times at 10,000 *g* for 5 min at 4°C. 2 µl of the LD fraction was diluted 10 times with buffer B and stained with LipidTOX for 20 min, then observed and captured by a high-resolution laser confocal microscopic (LSM800; Carl ZEISS) with a Plan-Apochromat 63×/1.4 Oil DIC objective and PMT and GaAsP detectors.

Western blot analysis

Young adult worms were collected in M9 buffer and quickly washed several times on ice, then quickly frozen with liquid nitrogen and stored at −80°C for later use. Each worm sample was lysed and homogenized in moderate high-salt radioimmunoprecipitation assay (RIPA) at 4°C. The homogenates were then centrifuged at 15,000 *g* for 10 min and the supernatant was used to determine the total protein concentration using the bicinchoninic acid assay (23225; Thermo Fisher Scientific). Lysates were diluted in 2× SDS sample buffer (100 mM Tris-HCl [pH6.8], 20% glycerin, 4% SDS, 0.2% bromophenol blue, 3% DTT) containing β-mercaptoethanol and boiled at 95°C for 5 min. For the LD protein isolation, the LD fraction was precipitated using 100% acetone, the proteins were collected by centrifugation at 13,000 *g* for 10 min. Then protein pellets were dissolved in 2× SDS sample buffer and boiled at 95°C for 5 min (Zhang et al., 2012). The proteins were separated by 10% SDS-PAGE gel and then transferred to polyvinylidene difluoride membranes at 0.25 A for 100 min on ice. The primary antibodies were rabbit anti-GFP antibody (ab6556; Abcam), rabbit anti-RFP antibody (ab62341; Abcam), mouse anti-FLAG antibody (F3165; Sigma-Aldrich), and rabbit anti-DHS-3 antibody (provided by Pingsheng Liu's lab) at 1:1,000 dilutions, and mouse anti-BIP antibody (66574-1-LG; Proteintech) and mouse anti-ACTIN-β (A5441; Sigma-Aldrich) at 1:2,500 dilutions. The secondary antibodies were goat anti-rabbit (31460; Invitrogen) and goat anti-mouse IgG (A24512; Thermo Fisher Scientific) at 1:5,000 dilutions. Images were captured with SageCapture (Sage), and analyzed by LANE 1D (Sage).

Fluorescence visualization

At least 200 GFP or RFP young adult worms were mounted on an agarose pad and anesthetized with 10 mM sodium azide. GFP or RFP fluorescence was visualized under a fluorescence microscope (BX53; Olympus) equipped with a CCD (DP74; Olympus) camera using cellSens standard software (version 4.1; Olympus) or ZEISS Axio Imager M2 (Carl ZEISS) equipped with a Axiocam 506 mono camera and controlled by ZEN 3.0 software (Carl Zeiss). Fluorescence reporter expression was quantified using ImageJ 1.53c. At least 10 worms were used for each biological sample. For the observation of subcellular structure, the worms with GFP, RFP, and mCherry were imaged by high-resolution laser confocal microscopy (LSM800; Carl ZEISS) with identical settings unless specifically indicated. Images were acquired with a Plan-Apochromat 63×/1.4 Oil DIC objective and PMT and GaAsP detectors. Images were processed and analyzed with ZEN 3.0 software, blue edition (Carl Zeiss). Images were taken from similar regions in the middle of intestine in young adult worms, unless specifically indicated.

Worms for RNA-Seq

About 40,000 synchronized L1 worms were transferred onto NGM plates seeded with the Con or the *let-767*RNAi bacteria. Once worms reached the L4 larval stage, the animals were collected, washed, and immediately frozen in liquid nitrogen for later use. Total RNA was extracted using RNAiso Plus. Subsequently, the following work was done by the Novogene Company. Generally, RNA quality was assessed by determining its RNA integrity number. A total amount of 1.5 µg RNA per sample was used as input material for the RNA sample preparations. Sequencing libraries were generated using NEBNextUltraTM RNA Library Prep Kit for Illumina (NEB) following the manufacturer's recommendations, and index codes were added to attribute sequences to each sample.

Co-IP analysis and IP-MS analysis

The lysates of transgenic worms were prepared using RIPA lysis buffer (P0013; Beyotime) containing protease inhibitor cocktail and phenylmethylsulfonyl fluoride. The worm lysates were centrifuged at 13,000 *g* for 10 min at 4°C. IP was performed by adding primary rabbit anti-RFP antibody (ab62314; Abcam), mouse anti-FLAG antibody (F3165; Sigma-Aldrich), or rabbit anti-GFP antibody (ab290; Abcam) to the worm lysates and then rocking overnight at 4°C. The immunoprecipitated samples were paired with the species-matched mouse IgG (12-371; Sigma-Aldrich) or rabbit IgG (ab172730; Abcam) as a negative Con. The worm lysates then were incubated with protein G agarose (20398; Thermo Fisher Scientific) to bind murine primary antibody or protein A agarose (ab193255; Abcam) to bind rabbit primary antibody and rocked for 6 h at 4°C. After washing four times with the washing buffer (50 mM Tris-HCl [pH 7.4], 150 mM NaCl, 0.5% NP-40, 1 mM EDTA, 0.25% sodium deoxycholate, ddH_2O), the immunoprecipitate was resuspended in a 2× SDS sample buffer and boiled at 95°C for 5 min for later western blot analysis or IP-MS analysis. Identification of protein adhesive strip by MS (Novogene Company).

Quantification and statistical analysis

Data are presented as the means ± SD unless specifically indicated; error bars in figures represent SD for at least triplicate experiments. Statistical analysis was performed by Student's *t* test for comparison between the means of two groups or by a one-way analysis of variance (ANOVA) with more than two groups. For all quantifications, the P values are represented for each statistical test, where $^{*}P < 0.05$, $^{**}P < 0.01$, $^{***}P < 0.001$, $^{\#}P < 0.05$, $^{\#\#}P < 0.01$, $^{\#\#\#}P < 0.001$, and ns for no significance. All figures were generated using GraphPad Prism 6 (GraphPad Software) and Photoshop CS5.

Online supplemental material

Fig. S1 shows the identification of *let-767* mutations and LET-767::GFP expression. Fig. S2 shows that RNAi reduction of *fat-6* or *acs-1* did not affect LD protein targeting. Fig. S3 shows that LET-767 deficiency–caused LD protein displacement was not due to activated lysosome. Fig. S4 shows LET-767::GFP IP-MS and ARF-1::RFP expression. Fig. S5 shows that RNAi reduction of *fat-6* and *acs-1* did not affect the localization of ARF-1::RFP and ATGL-1::GFP. Table S1 lists the worm strains used in this study. Table S2 shows the 51 candidate genes. Table S3 shows the RNA-Seq analysis of WT;*let-767*RNAi via pathway enrichment. Table S4 lists proteins interacting with LET-767 detected by IP-MS.

Data availability

The data that support the findings of this study are available from the corresponding authors upon reasonable request.

Acknowledgments

We thank Dr. Leonard Krall for the English copyediting.

This work was supported by Yunnan Provincial Science and Technology Project at Southwest United Graduate School (202302AO370004), the National Natural Science Foundation of China (32071281, 32371232, 82360726, 32360161, 32160155, 32000818, 32360221, 82300972), the Ministry of Science and Technology of the People's Republic of China (2018YFA0800700, 2018YFA0800703), the Yunnan Fundamental Research Projects (202301BF070001-023, 202301AT070123, 202101AT070009, 202401AS070146), and the China Postdoctoral Science Foundation (2023M731447).

Author contributions: B. Liang and L. Fu conceived and designed the experiments. B. Liang, L. Fu, and Y. Wang wrote the paper. L. Fu, J. Zhang, Y. Wang, and H. Wu performed most of the experiments and data analysis. X. Xu and H. Wang provided some technical methods, and J. Zhang and Y. Wang performed partial RNAi screening. X. Zou, X. Jiang, J. Li, J. Liu, C. Li, Z. Li, Y. He, Y. Wu, and P. Liu provided guidance for some experiments and contributed reagents/materials/analysis tools and revised the manuscript. B. Liang initiated the project. All authors reviewed the manuscript.

Disclosures: The authors declare no competing interests exist.

Submitted: 6 November 2023
Revised: 22 February 2024
Accepted: 12 March 2024

References

Bartz, R., W.H. Li, B. Venables, J.K. Zehmer, M.R. Roth, R. Welti, R.G.W. Anderson, P. Liu, and K.D. Chapman. 2007. Lipidomics reveals that adiposomes store ether lipids and mediate phospholipid traffic. *J. Lipid Res.* 48:837–847. https://doi.org/10.1194/jlr.M600413-JLR200

Beller, M., C. Sztalryd, N. Southall, M. Bell, H. Jäckle, D.S. Auld, and B. Oliver. 2008. COPI complex is a regulator of lipid homeostasis. *PLoS Biol.* 6: e292. https://doi.org/10.1371/journal.pbio.0060292

Bersuker, K., and J.A. Olzmann. 2017. Establishing the lipid droplet proteome: Mechanisms of lipid droplet protein targeting and degradation. *Biochim. Biophys. Acta Mol. Cell Biol. Lipids*. 1862:1166–1177. https://doi.org/10.1016/j.bbalip.2017.06.006

Blanchette-Mackie, E.J., N.K. Dwyer, T. Barber, R.A. Coxey, T. Takeda, C.M. Rondinone, J.L. Theodorakis, A.S. Greenberg, and C. Londos. 1995. Perilipin is located on the surface layer of intracellular lipid droplets in adipocytes. *J. Lipid Res.* 36:1211–1226. https://doi.org/10.1016/S0022-2275(20)41129-0

Brock, T.J., J. Browse, and J.L. Watts. 2006. Genetic regulation of unsaturated fatty acid composition in *C. elegans*. *PLoS Genet*. 2. e108. https://doi.org/10.1371/journal.pgen.0020108

Brock, T.J., J. Browse, and J.L. Watts. 2007. Fatty acid desaturation and the regulation of adiposity in *Caenorhabditis elegans*. *Genetics*. 176:865–875. https://doi.org/10.1534/genetics.107.071860

Cermelli, S., Y. Guo, S.P. Gross, and M.A. Welte. 2006. The lipid-droplet proteome reveals that droplets are a protein-storage depot. *Curr. Biol.* 16:1783–1795. https://doi.org/10.1016/j.cub.2006.07.062

Desnoyers, S., P.G. Blanchard, J.F. St-Laurent, S.N. Gagnon, D.L. Baillie, and V. Luu-The. 2007. *Caenorhabditis elegans* LET-767 is able to metabolize androgens and estrogens and likely shares common ancestor with human types 3 and 12 17beta-hydroxysteroid dehydrogenases. *J. Endocrinol.* 195:271–279. https://doi.org/10.1677/JOE-07-0248

Ding, Y., Y. Wu, R. Zeng, and K. Liao. 2012. Proteomic profiling of lipid droplet-associated proteins in primary adipocytes of normal and obese mouse. *Acta Biochim. Biophys. Sin.* 44:394–406. https://doi.org/10.1093/abbs/gms008

Egan, J.J., A.S. Greenberg, M.K. Chang, S.A. Wek, M.C. Moos Jr., and C. Londos. 1992. Mechanism of hormone-stimulated lipolysis in adipocytes: Translocation of hormone-sensitive lipase to the lipid storage droplet. *Proc. Natl. Acad. Sci. USA*. 89:8537–8541. https://doi.org/10.1073/pnas.89.18.8537

Ellong, E.N., K.G. Soni, Q.T. Bui, R. Sougrat, M.P. Golinelli-Cohen, and C.L. Jackson. 2011. Interaction between the triglyceride lipase ATGL and the

Arf1 activator GBF1. *PLoS One*. 6:e21889. https://doi.org/10.1371/journal.pone.0021889

Enkler, L., V. Szentgyörgyi, M. Pennauer, C. Prescianotto-Baschong, I. Riezman, A. Wiesyk, R.E. Avraham, M. Spiess, E. Zalckvar, R. Kucharczyk, et al. 2023. Arf1 coordinates fatty acid metabolism and mitochondrial homeostasis. *Nat. Cell Biol.* 25:1157–1172. https://doi.org/10.1038/s41556-023-01180-2

Entchev, E.V., D. Schwudke, V. Zagoriy, V. Matyash, A. Bogdanova, B. Habermann, L. Zhu, A. Shevchenko, and T.V. Kurzchalia. 2008. LET-767 is required for the production of branched chain and long chain fatty acids in *Caenorhabditis elegans*. *J. Biol. Chem.* 283:17550–17560. https://doi.org/10.1074/jbc.M800965200

Frøkjaer-Jensen, C., M.W. Davis, C.E. Hopkins, B.J. Newman, J.M. Thummel, S.P. Olesen, M. Grunnet, and E.M. Jorgensen. 2008. Single-copy insertion of transgenes in *Caenorhabditis elegans*. *Nat. Genet.* 40:1375–1383. https://doi.org/10.1038/ng.248

Fujimoto, T., H. Kogo, K. Ishiguro, K. Tauchi, and R. Nomura. 2001. Caveolin-2 is targeted to lipid droplets, a new "membrane domain" in the cell. *J. Cell Biol.* 152:1079–1085. https://doi.org/10.1083/jcb.152.5.1079

Fujimoto, Y., H. Itabe, J. Sakai, M. Makita, J. Noda, M. Mori, Y. Higashi, S. Kojima, and T. Takano. 2004. Identification of major proteins in the lipid droplet-enriched fraction isolated from the human hepatocyte cell line HuH7. *Biochim. Biophys. Acta*. 1644:47–59. https://doi.org/10.1016/j.bbamcr.2003.10.018

Gallardo-Montejano, V.I., G. Saxena, C.M. Kusminski, C. Yang, J.L. McAfee, L. Hahner, K. Hoch, W. Dubinsky, V.A. Narkar, and P.E. Bickel. 2016. Nuclear Perilipin 5 integrates lipid droplet lipolysis with PGC-1α/SIRT1-dependent transcriptional regulation of mitochondrial function. *Nat. Commun.* 7:12723. https://doi.org/10.1038/ncomms12723

Gao, M., X. Huang, B.L. Song, and H. Yang. 2019. The biogenesis of lipid droplets: Lipids take center stage. *Prog. Lipid Res.* 75:100989. https://doi.org/10.1016/j.plipres.2019.100989

Garcia, G., H. Zhang, S. Moreno, C.K. Tsui, B.M. Webster, R. Higuchi-Sanabria, A. Dillin, and R.Y. Hampton. 2023. Lipid homeostasis is essential for a maximal ER stress response. *Elife*. 12:e83884. https://doi.org/10.7554/eLife.83884

Gong, J., Z. Sun, L. Wu, W. Xu, N. Schieber, D. Xu, G. Shui, H. Yang, R.G. Parton, and P. Li. 2011. Fsp27 promotes lipid droplet growth by lipid exchange and transfer at lipid droplet contact sites. *J. Cell Biol.* 195:953–963. https://doi.org/10.1083/jcb.201104142

Greenberg, A.S., J.J. Egan, S.A. Wek, N.B. Garty, E.J. Blanchette-Mackie, and C. Londos. 1991. Perilipin, a major hormonally regulated adipocyte-specific phosphoprotein associated with the periphery of lipid storage droplets. *J. Biol. Chem.* 266:11341–11346. https://doi.org/10.1016/S0021-9258(18)99168-4

Greenwood, D.J., M.S. Dos Santos, S. Huang, M.R.G. Russell, L.M. Collinson, J.I. MacRae, A. West, H. Jiang, and M.G. Gutierrez. 2019. Subcellular antibiotic visualization reveals a dynamic drug reservoir in infected macrophages. *Science*. 364:1279–1282. https://doi.org/10.1126/science.aat9689

Kory, N., R.V. Farese Jr., and T.C. Walther. 2016. Targeting fat: Mechanisms of protein localization to lipid droplets. *Trends Cell Biol.* 26:535–546. https://doi.org/10.1016/j.tcb.2016.02.007

Krahmer, N., Y. Guo, F. Wilfling, M. Hilger, S. Lingrell, K. Heger, H.W. Newman, M. Schmidt-Supprian, D.E. Vance, M. Mann, et al. 2011. Phosphatidylcholine synthesis for lipid droplet expansion is mediated by localized activation of CTP:phosphocholine cytidylyltransferase. *Cell Metab.* 14:504–515. https://doi.org/10.1016/j.cmet.2011.07.013

Kuervers, L.M., C.L. Jones, N.J. O'Neil, and D.L. Baillie. 2003. The sterol modifying enzyme LET-767 is essential for growth, reproduction and development in *Caenorhabditis elegans*. *Mol. Genet. Genomics*. 270:121–131. https://doi.org/10.1007/s00438-003-0900-9

Lee, J.H., J. Kong, J.Y. Jang, J.S. Han, Y. Ji, J. Lee, and J.B. Kim. 2014. Lipid droplet protein LID-1 mediates ATGL-1-dependent lipolysis during fasting in *Caenorhabditis elegans*. *Mol. Cell. Biol.* 34:4165–4176. https://doi.org/10.1128/MCB.00722-14

Liu, Y., S. Xu, C. Zhang, X. Zhu, M.A. Hammad, X. Zhang, M. Christian, H. Zhang, and P. Liu. 2018. Hydroxysteroid dehydrogenase family proteins on lipid droplets through bacteria, *C. elegans*, and mammals. *Biochim. Biophys. Acta Mol. Cell Biol. Lipids*. 1863:881–894. https://doi.org/10.1016/j.bbalip.2018.04.018

Mauvezin, C., and T.P. Neufeld. 2015. Bafilomycin A1 disrupts autophagic flux by inhibiting both V-ATPase-dependent acidification and Ca-P60A/SERCA-dependent autophagosome-lysosome fusion. *Autophagy*. 11:1437–1438. https://doi.org/10.1080/15548627.2015.1066957

Mejhert, N., L. Kuruvilla, K.R. Gabriel, S.D. Elliott, M.A. Guie, H. Wang, Z.W. Lai, E.A. Lane, R. Christiano, N.N. Danial, et al. 2020. Partitioning of MLX-Family transcription factors to lipid droplets regulates metabolic gene expression. *Mol. Cell*. 77:1251–1264.e9. https://doi.org/10.1016/j.molcel.2020.01.014

Miyanari, Y., K. Atsuzawa, N. Usuda, K. Watashi, T. Hishiki, M. Zayas, R. Bartenschlager, T. Wakita, M. Hijikata, and K. Shimotohno. 2007. The lipid droplet is an important organelle for hepatitis C virus production. *Nat. Cell Biol.* 9:1089–1097. https://doi.org/10.1038/ncb1631

Na, H., P. Zhang, Y. Chen, X. Zhu, Y. Liu, Y. Liu, K. Xie, N. Xu, F. Yang, Y. Yu, et al. 2015. Identification of lipid droplet structure-like/resident proteins in *Caenorhabditis elegans*. *Biochim. Biophys. Acta*. 1853:2481–2491. https://doi.org/10.1016/j.bbamcr.2015.05.020

Olarte, M.J., J.M.J. Swanson, T.C. Walther, and R.V. Farese Jr. 2022. The CYTOLD and ERTOLD pathways for lipid droplet-protein targeting. *Trends Biochem. Sci.* 47:39–51. https://doi.org/10.1016/j.tibs.2021.08.007

Ostermeyer, A.G., J.M. Paci, Y. Zeng, D.M. Lublin, S. Munro, and D.A. Brown. 2001. Accumulation of caveolin in the endoplasmic reticulum redirects the protein to lipid storage droplets. *J. Cell Biol.* 152:1071–1078. https://doi.org/10.1083/jcb.152.5.1071

Prévost, C., M.E. Sharp, N. Kory, Q. Lin, G.A. Voth, R.V. Farese Jr., and T.C. Walther. 2018. Mechanism and determinants of amphipathic helix-containing protein targeting to lipid droplets. *Dev. Cell*. 44:73–86.e4. https://doi.org/10.1016/j.devcel.2017.12.011

Roberts, M.A., and J.A. Olzmann. 2020. Protein quality control and lipid droplet metabolism. *Annu. Rev. Cell Dev. Biol.* 36:115–139. https://doi.org/10.1146/annurev-cellbio-031320-101827

Rowe, E.R., M.L. Mimmack, A.D. Barbosa, A. Haider, I. Isaac, M.M. Ouberai, A.R. Thiam, S. Patel, V. Saudek, S. Siniossoglou, and D.B. Savage. 2016. Conserved amphipathic helices mediate lipid droplet targeting of perilipins 1-3. *J. Biol. Chem.* 291:6664–6678. https://doi.org/10.1074/jbc.M115.691048

Schott, M.B., S.G. Weller, R.J. Schulze, E.W. Krueger, K. Drizyte-Miller, C.A. Casey, and M.A. McNiven. 2019. Lipid droplet size directs lipolysis and lipophagy catabolism in hepatocytes. *J. Cell Biol.* 218:3320–3335. https://doi.org/10.1083/jcb.201803153

Smirnova, E., E.B. Goldberg, K.S. Makarova, L. Lin, W.J. Brown, and C.L. Jackson. 2006. ATGL has a key role in lipid droplet/adiposome degradation in mammalian cells. *EMBO Rep.* 7:106–113. https://doi.org/10.1038/sj.embor.7400559

Soni, K.G., G.A. Mardones, R. Sougrat, E. Smirnova, C.L. Jackson, and J.S. Bonifacino. 2009. Coatomer-dependent protein delivery to lipid droplets. *J. Cell Sci.* 122:1834–1841. https://doi.org/10.1242/jcs.045849

Stone, S.J., M.C. Levin, and R.V. Farese Jr. 2006. Membrane topology and identification of key functional amino acid residues of murine acyl-CoA:diacylglycerol acyltransferase-2. *J. Biol. Chem.* 281:40273–40282. https://doi.org/10.1074/jbc.M607986200

Suzuki, M., T. Murakami, J. Cheng, H. Kano, M. Fukata, and T. Fujimoto. 2015. ELMOD2 is anchored to lipid droplets by palmitoylation and regulates adipocyte triglyceride lipase recruitment. *Mol. Biol. Cell*. 26:2333–2342. https://doi.org/10.1091/mbc.E14-11-1504

Sztalryd, C., and D.L. Brasaemle. 2017. The perilipin family of lipid droplet proteins: Gatekeepers of intracellular lipolysis. *Biochim. Biophys. Acta Mol. Cell Biol. Lipids*. 1862:1221–1232. https://doi.org/10.1016/j.bbalip.2017.07.009

Sztalryd, C., G. Xu, H. Dorward, J.T. Tansey, J.A. Contreras, A.R. Kimmel, and C. Londos. 2003. Perilipin A is essential for the translocation of hormone-sensitive lipase during lipolytic activation. *J. Cell Biol.* 161:1093–1103. https://doi.org/10.1083/jcb.200210169

Thompson, O., M. Edgley, P. Strasbourger, S. Flibotte, B. Ewing, R. Adair, V. Au, I. Chaudhry, L. Fernando, H. Hutter, et al. 2013. The million mutation project: A new approach to genetics in *Caenorhabditis elegans*. *Genome Res.* 23:1749–1762. https://doi.org/10.1101/gr.157651.113

Vrablik, T.L., V.A. Petyuk, E.M. Larson, R.D. Smith, and J.L. Watts. 2015. Lipidomic and proteomic analysis of *Caenorhabditis elegans* lipid droplets and identification of ACS-4 as a lipid droplet-associated protein. *Biochim. Biophys. Acta*. 1851:1337–1345. https://doi.org/10.1016/j.bbalip.2015.06.004

Watts, J.L., and M. Ristow. 2017. Lipid and carbohydrate metabolism in *Caenorhabditis elegans*. *Genetics*. 207:413–446. https://doi.org/10.1534/genetics.117.300106

Wilfling, F., H. Wang, J.T. Haas, N. Krahmer, T.J. Gould, A. Uchida, J.X. Cheng, M. Graham, R. Christiano, F. Fröhlich, et al. 2013. Triacylglycerol synthesis enzymes mediate lipid droplet growth by relocalizing from the ER to lipid droplets. *Dev. Cell*. 24:384–399. https://doi.org/10.1016/j.devcel.2013.01.013

Wilfling, F., A.R. Thiam, M.J. Olarte, J. Wang, R. Beck, T.J. Gould, E.S. Allgeyer, F. Pincet, J. Bewersdorf, R.V. Farese Jr., and T.C. Walther. 2014. Arf1/COPI machinery acts directly on lipid droplets and enables their connection to the ER for protein targeting. *Elife*. 3:e01607. https://doi.org/10.7554/eLife.01607

Wu, J., X. Jiang, Y. Li, T. Zhu, J. Zhang, Z. Zhang, L. Zhang, Y. Zhang, Y. Wang, X. Zou, et al. 2018. PHA-4/FoxA senses nucleolar stress to regulate lipid accumulation in *Caenorhabditis elegans*. *Nat. Commun*. 9:1195. https://doi.org/10.1038/s41467-018-03531-2

Xu, N., S.O. Zhang, R.A. Cole, S.A. McKinney, F. Guo, J.T. Haas, S. Bobba, R.V. Farese Jr., and H.Y. Mak. 2012. The FATP1-DGAT2 complex facilitates lipid droplet expansion at the ER-lipid droplet interface. *J. Cell Biol*. 198: 895–911. https://doi.org/10.1083/jcb.201201139

Yang, R., Y. Li, Y. Wang, J. Zhang, Q. Fan, J. Tan, W. Li, X. Zou, and B. Liang. 2022. NHR-80 senses the mitochondrial UPR to rewire citrate metabolism for lipid accumulation in *Caenorhabditis elegans*. *Cell Rep*. 38: 110206. https://doi.org/10.1016/j.celrep.2021.110206

Yokoi, Y., Y. Horiguchi, M. Araki, and K. Motojima. 2007. Regulated expression by PPARalpha and unique localization of 17beta-hydroxysteroid dehydrogenase type 11 protein in mouse intestine and liver. *FEBS J*. 274:4837–4847. https://doi.org/10.1111/j.1742-4658.2007.06005.x

Zadoorian, A., X. Du, and H. Yang. 2023. Lipid droplet biogenesis and functions in health and disease. *Nat. Rev. Endocrinol*. 19:443–459. https://doi.org/10.1038/s41574-023-00845-0

Zhang, C., and P. Liu. 2019. The new face of the lipid droplet: Lipid droplet proteins. *Proteomics*. 19:e1700223. https://doi.org/10.1002/pmic.201700223

Zhang, H., N. Abraham, L.A. Khan, D.H. Hall, J.T. Fleming, and V. Göbel. 2011. Apicobasal domain identities of expanding tubular membranes depend on glycosphingolipid biosynthesis. *Nat. Cell Biol*. 13:1189–1201. https://doi.org/10.1038/ncb2328

Zhang, P., H. Na, Z. Liu, S. Zhang, P. Xue, Y. Chen, J. Pu, G. Peng, X. Huang, F. Yang, et al. 2012. Proteomic study and marker protein identification of *Caenorhabditis elegans* lipid droplets. *Mol. Cell. Proteomics*. 11:317–328. https://doi.org/10.1074/mcp.M111.016345

Zhang, Y., X. Zou, Y. Ding, H. Wang, X. Wu, and B. Liang. 2013. Comparative genomics and functional study of lipid metabolic genes in *Caenorhabditis elegans*. *BMC Genomics*. 14:164. https://doi.org/10.1186/1471-2164-14-164

Zhang, J., Y. Hu, Y. Wang, L. Fu, X. Xu, C. Li, J. Xu, C. Li, L. Zhang, R. Yang, et al. 2021. mmBCFA C17iso ensures endoplasmic reticulum integrity for lipid droplet growth. *J. Cell Biol*. 220:e202102122. https://doi.org/10.1083/jcb.202102122

Supplemental material

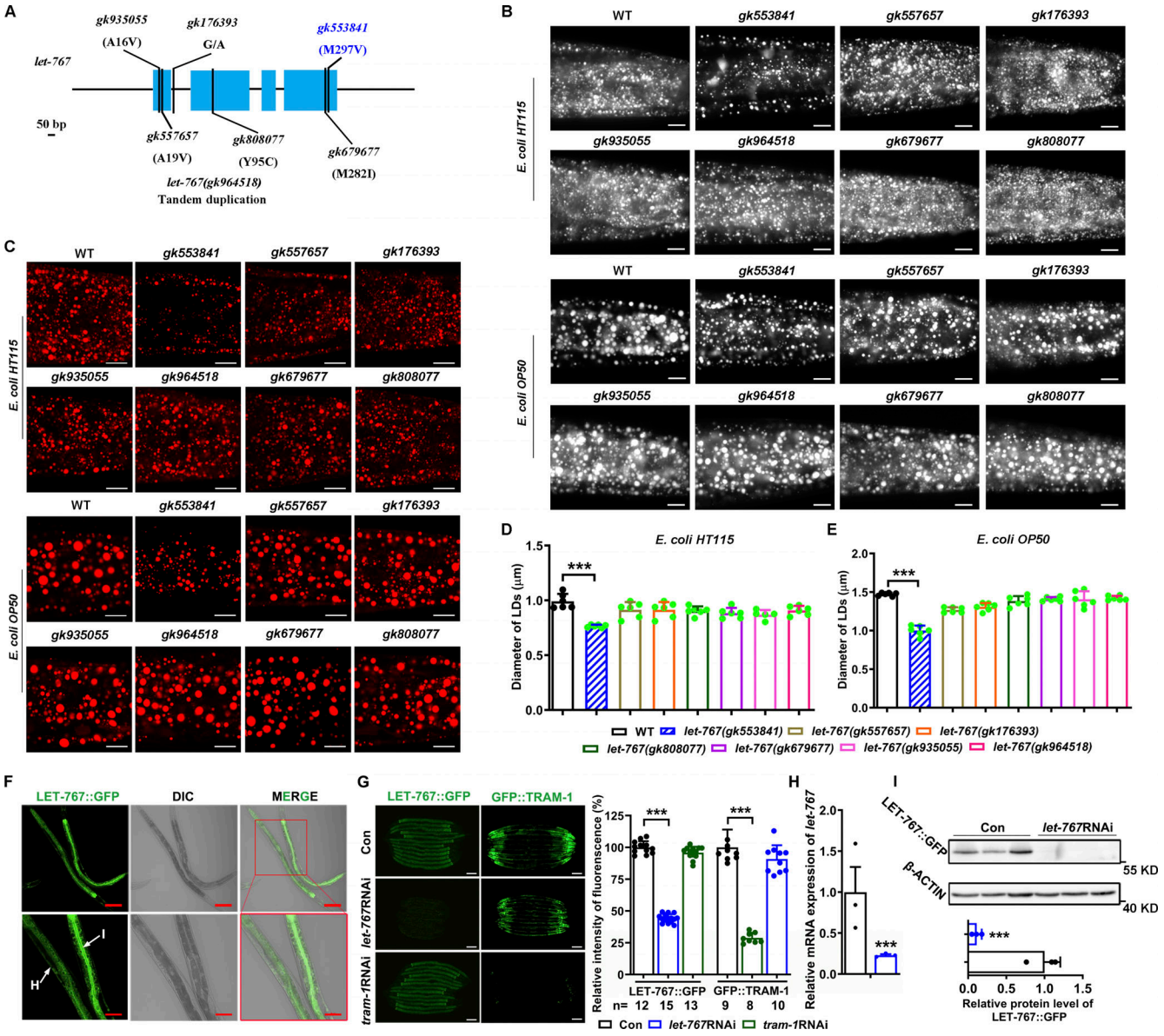

Figure S1. **Identification of *let-767* mutations and LET-767::GFP expression. (A)** The structure diagram of the *let-767* gene. Genetic variants are listed on the panel and also in Table S1. Scale bar represents 50 bp. **(B and C)** Nile Red staining (B) and LipidTOX staining (C) of LDs in fixed worms, cultivated on *E. coli* HT115 or OP50, respectively. The scale bar represents 10 μm. **(D and E)** Quantification of LD diameters from C. Data are presented as the mean ± SD of six representative animals for each worm strain. **(F)** Fluorescence microscopy of LET-767::GFP. The scale bar represents 100 μm for top panel, and 50 μm for bottom panel. I and H indicate intestine and hypodermis, respectively. **(G)** Fluorescence intensity and quantification of LET-767::GFP and GFP::TRAM-1 in indicated worms. The scale bar represents 100 μm. *n*, the number of measured worms for each worm strain. **(H)** Relative mRNA level of *let-767* by qPCR analysis. Data are presented as the mean ± SD of three biological repeats for each worm strain. **(I)** Top: Western blot analysis of LET-767::GFP using anti-GFP antibody. Bottom: The relative protein level of LET-767::GFP normalized by β-ACTIN as an internal Con. Data are presented as the mean ± SD of three biological repeats for each worm strain. Significant difference between two indicated worms or between Con and a specific RNAi treatment, ***P < 0.001 by two-tailed *t* test. For all representative animals, anterior is left and posterior is right. Images in C were taken by confocal microscopy (ZEISS, Carl LSM800), while B, F, and G were taken by ZEISS Axio Imager M2 microscopy. Source data are available for this figure: SourceData FS1.

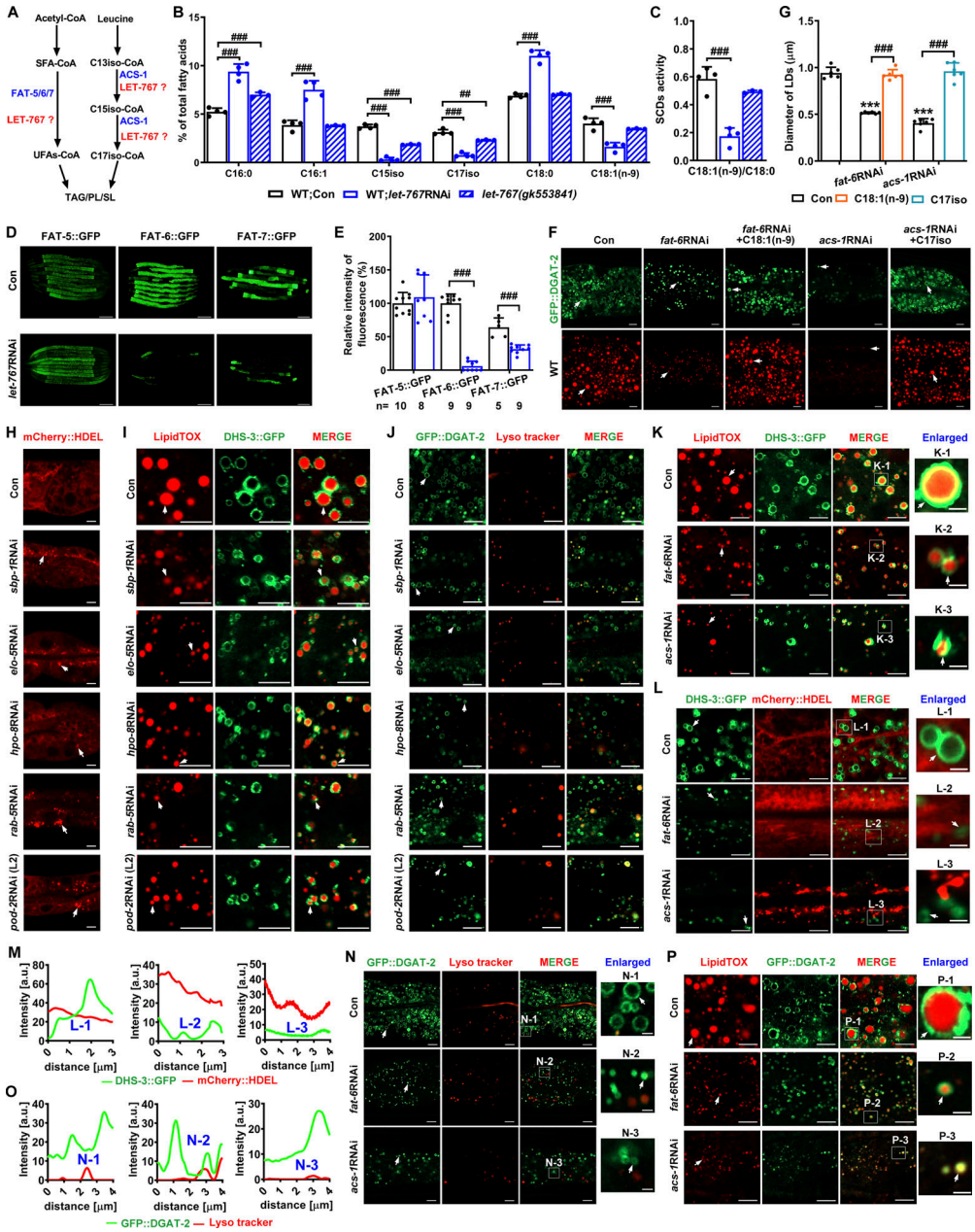

Figure S2. **RNAi reduction of *fat-6* or *acs-1* did not affect LD protein targeting. (A)** Schematic diagram of LET-767 in the biosynthesis of monomethyl-branched chain fatty acids (mmBCFAs) and unsaturated fatty acids (UFAs) in *C. elegans*. SFA, saturated fatty acid; PUFAs, polyunsaturated fatty acids; SL, sphingolipids. **(B)** Percentage of the C16:0, C16:1, C15iso, C17iso, C18:0, and C18:1(n-9) in total fatty acids. **(C)** SCD activity indicated by the ratio of C18:1(n-9)/C18:0. **(B and C)** Data are presented as the mean ± SD of four biological repeats for each worm strain. **(D and E)** Fluorescence intensity (D) and quantification (E) of FAT-5::GFP, FAT-6::GFP, and FAT-7:: GFP. The scale bar represents 20 μm. Data are presented as the mean ± SD. *n*, the number of measured worms for each worm strain. Images were taken by OLYMPUS BX53 microscopy. **(F)** Visualization of LDs by LipidTOX staining and LD marker GFP::DGAT-2. White arrows indicate LDs. **(G)** Quantification of LD diameter from F. Data are presented as the mean ± SD of six representative animals for each worm strain. **(H)** Representative images of the ER morphology indicated by mCherry::HDEL. White arrows indicated the aggregation of the ER. **(I and J)** Localization of DHS-3::GFP and GFP::DGAT-2 with respect to LDs. LDs stained by LipidTOX Red (I), and lysosome was stained by Lyso tracker (J). White arrows indicate LDs. **(K)** Localization of DHS-3::GFP with respect to LDs stained by LipidTOX. White arrows indicate the localization of DHS-3::GFP on LDs. **(L)** Localization of DHS-3::GFP with respect to ER marked by mCherry::HDEL. White arrows indicate the localization of DHS-3::GFP on LDs. The scale bar represents 5 μm. **(M)** Intensity profiles of labeled scans from high-magnification regions, L-1, L-2, and L-3, show the localization of DHS-3::GFP with mCherry::HDEL found in L. **(N)** Localization of GFP::DGAT-2 on LDs. Lysosome was stained by Lyso tracker. White arrows indicate LDs. **(O)** Intensity profiles of labeled scans from high-magnification regions, N-1, N-2, and N-3, show the localization of GFP::DGAT-2 with Lyso tracker found in N. **(P)** Localization of GFP::DGAT-2 with respect to LDs stained by LipidTOX. White arrows indicate the localization of GFP::DGAT-2 on LDs. Significant difference between Con and RNAi, ***P < 0.001, significant difference between two indicated worms, ##P < 0.01, ###P < 0.001, the P values are indicated by two-tailed *t* test (E) and one-way ANOVA (B, C, and G). All fluorescence images were captured by high-resolution laser confocal microscopy (ZEISS, Carl LSM800), except D. For all of the represented animals, the anterior is on the left and the posterior is on the right. Scale bar represents 1 μm in enlarged panels and 5 μm in others, respectively, unless specifically indicated.

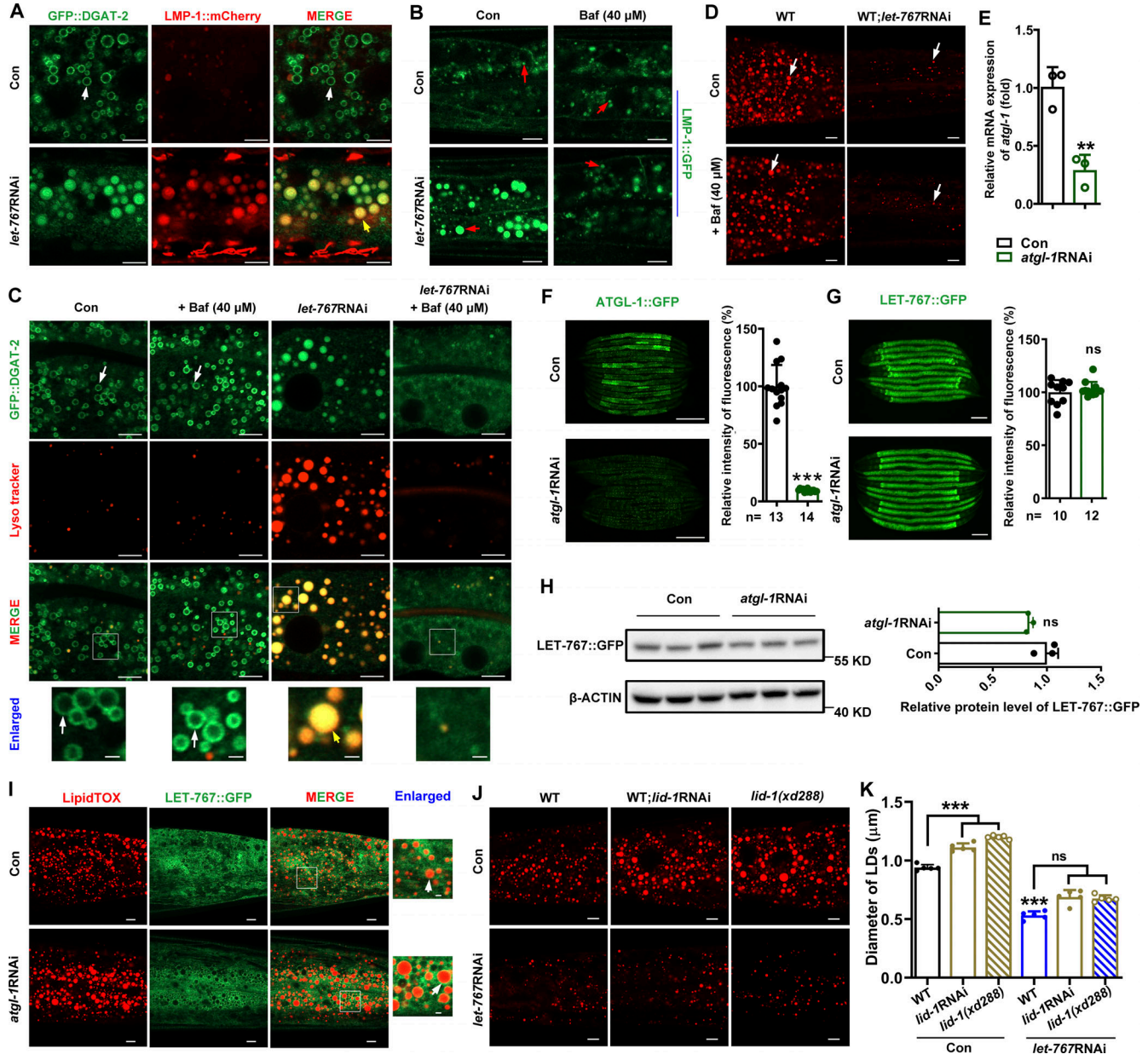

Figure S3. **LET-767 deficiency–caused LD protein displacement was not due to activated lysosome. (A)** Localization of GFP::DGAT-2 with respect to lysosome marked by LMP-1::mCherry. White arrows and yellow arrows indicate the localization of GFP::DGAT-2 on LDs and lysosome, respectively. **(B)** Visualization of the lysosome marker by LMP-1::GFP treated with 40 μM Bafilomycin A1 (Baf). Red arrows indicate lysosome. **(C)** Localization of GFP::DGAT-2 with respect to lysosome stained by Lyso tracker. White arrows indicate the localization of GFP::DGAT-2 on LDs, and yellow arrows indicate the localization of GFP::DGAT-2 on lysosome. **(D)** LipidTOX staining of LDs in fixed worms with/without Baf treatment. White arrows indicate LDs. **(E)** Relative mRNA level of *atgl-1* by qPCR analysis. **(F and G)** Fluorescence intensity (left) and quantification (right) of ATGL-1::GFP (F) and LET-767::GFP (G), respectively. Scale bar represents 100 μm. Data are presented as the mean ± SD. *n*, the number of measured worms for each worm strain. **(H)** Left: Western blot analysis of LET-767::GFP using anti-GFP antibody. Right: Quantification of LET-767::GFP normalized by β-ACTIN as an internal Con. **(E and H)** Data are presented as the mean ± SD of three biological repeats for each worm strain. **(I)** Localization of LET-767::GFP to LDs stained by LipidTOX. White arrows indicate LET-767::GFP on LDs. **(J and K)** LipidTOX staining (J) and quantification (K) of LDs in fixed worms. Data are presented as the mean ± SD of six representative animals for each worm strain. Significant difference between Con and an indicated RNAi or between WT and mutant, **P < 0.01, ***P < 0.001. ns, no significance. The P values are indicated by two-tailed *t*-test (E–H) and one-way ANOVA (K). All fluorescence images were captured by high-resolution laser confocal microscopy (ZEISS, Carl LSM800), except F and G taken by ZEISS Axio Imager M2 microscopy. Scale bar represents 1 μm in enlarged panels and 5 μm in others, respectively, unless specifically indicated. Source data are available for this figure: SourceData FS3.

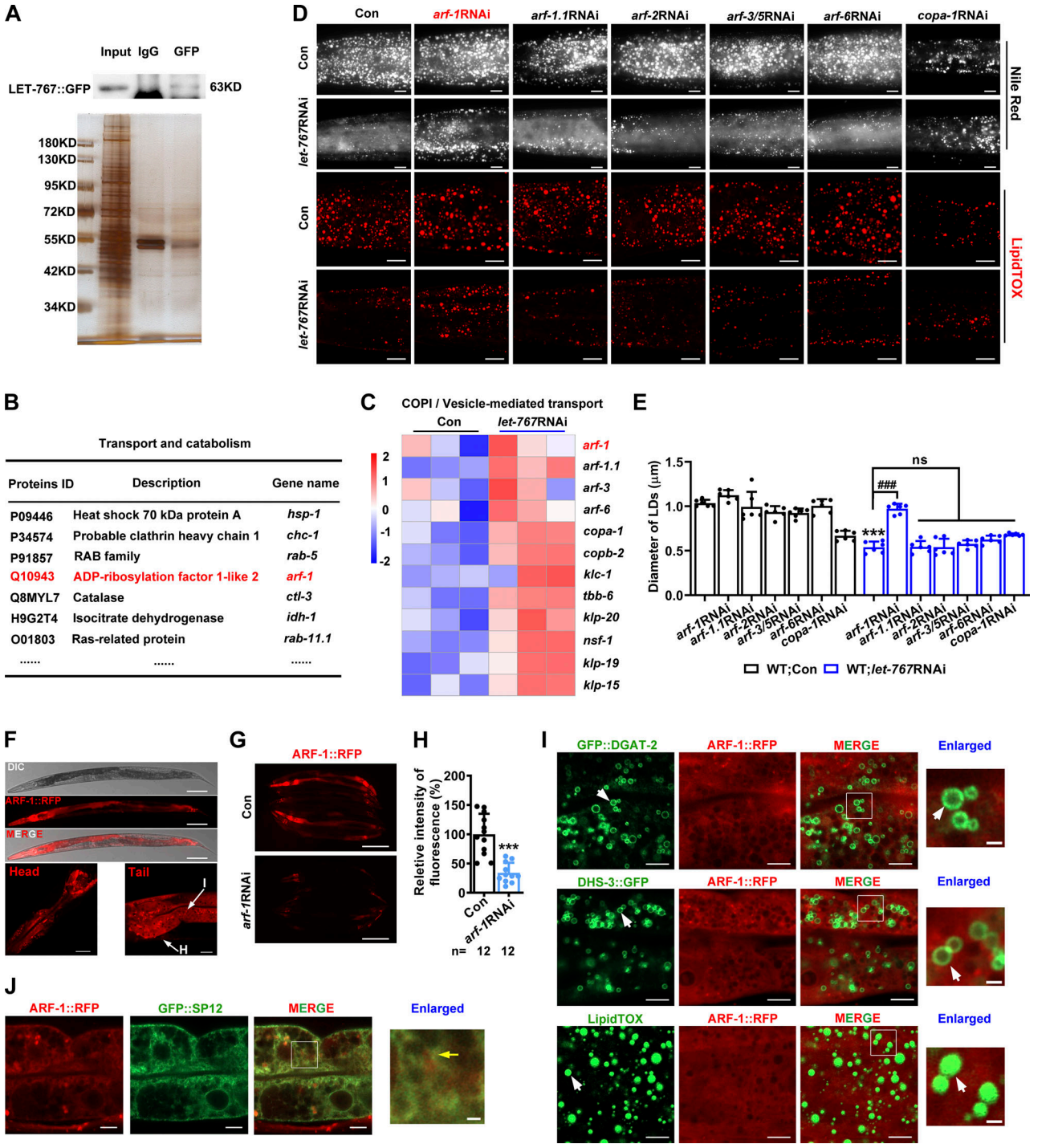

Figure S4. **LET-767::GFP IP-MS and ARF-1::RFP expression. (A)** Identification of LET-767::GFP interaction partners for MS via SDS-PAGE silver staining. **(B)** List of several LET-767 interacting proteins from IP-MS data. **(C)** Heat map of genes involved in COPI/vesicle-mediated transport pathway from RNA-Seq data. **(D)** Nile Red staining (taken by ZEISS Axio Imager M2 microscopy) and LipidTOX staining (taken by high-resolution laser confocal microscopy ZEISS LSM800) of LDs in fixed worms. Scale bar represents 10 μm. **(E)** Quantification of LD diameters from D. Data are presented as the mean ± SD of six representative animals for each worm strain. **(F)** Confocal microscopy of ARF-1::RFP. Scale bar represents 100 μm on the top panel, 20 μm for the left panel, and 10 μm for right panel. I, intestine; H, hypodermis. **(G and H)** Fluorescence intensity (G) and quantification (H) of ARF-1::RFP. Scale bar represents 200 μm. Images were taken by ZEISS Axio Imager M2 microscopy. Data are presented as the mean ± SD. *n*, the number of measured worms for each worm strain. **(I)** Localization of ARF-1::RFP with respect to LD marker GFP::DGAT-2, DHS-3::GFP, and LipidTOX staining LDs. Scale bars in merged and enlarged panels represent 5 and 1 μm, respectively. White arrows indicate LDs. **(J)** Localization of ARF-1::RFP with respect to GFP::SP12. Scale bars in merged and enlarged panels represent 5 and 1 μm, respectively. Yellow arrow indicates overlapped ARF-1::RFP with GFP::SP12. Significant difference between Con and a specific RNAi, ***P < 0.001, significant difference between two indicated worm strains, ###P < 0.001. ns, no significance; the P values are indicated by two-tailed *t* test (H) and one-way ANOVA (E). Images in F, I, and J were taken by high-resolution laser confocal microscopy (ZEISS, Carl LSM800). Source data are available for this figure: SourceData FS4.

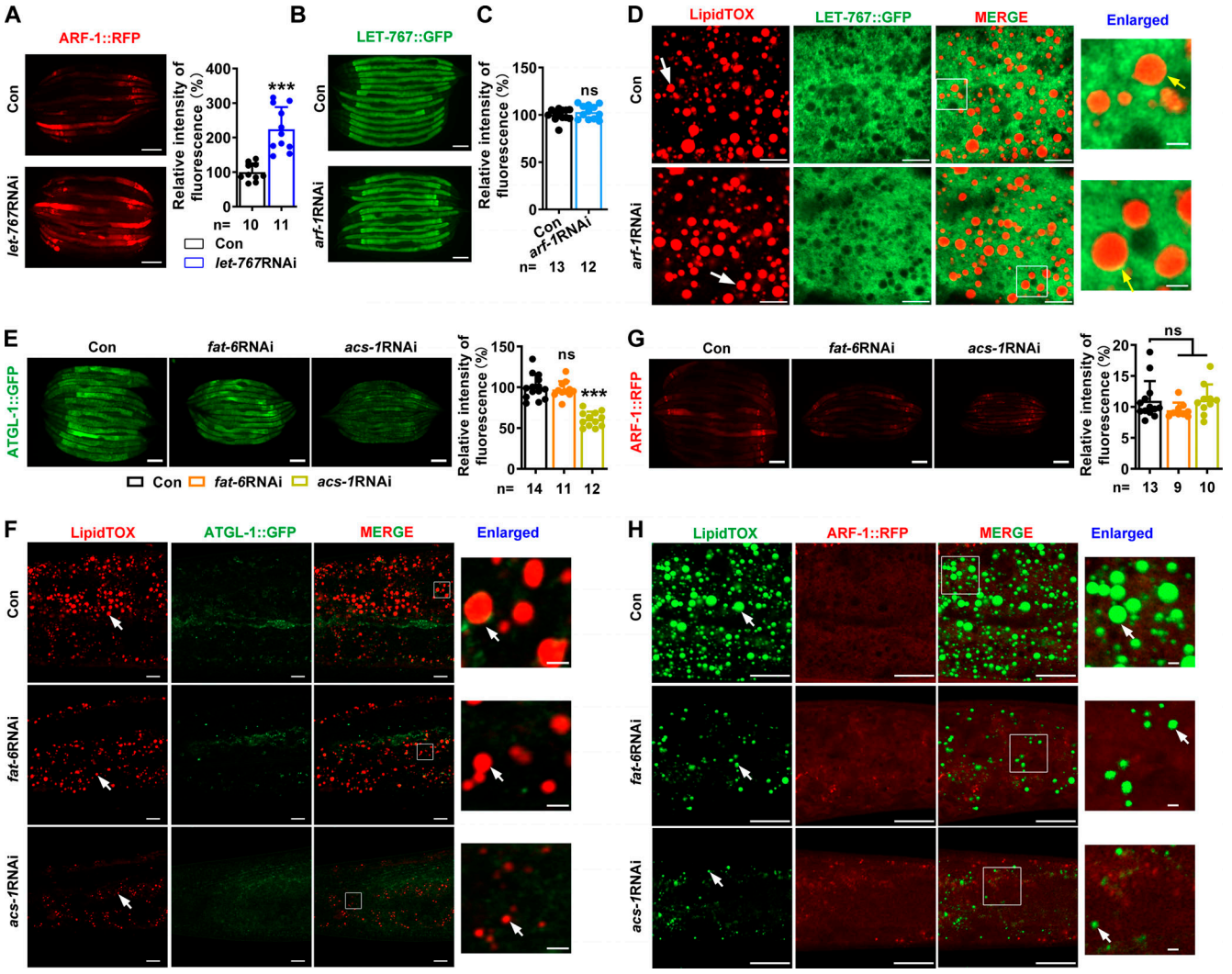

Figure S5. **RNAi reduction of *fat-6* and *acs-1* did not affect the localization of ARF-1::RFP and ATGL-1::GFP. (A)** Fluorescence intensity (left) and quantification (right) of ARF-1::RFP in Con and *let-767*RNAi. Scale bar represents 100 µm. **(B and C)** Fluorescence intensity (B) and quantification (C) of LET-767::GFP in Con and *arf-1*RNAi. Scale bar represents 100 µm. **(D)** Localization of LET-767::GFP on LDs stained by LipidTOX. White arrows indicate LDs and yellow arrows indicate the localization of LET-767::GFP on LDs. **(E)** Fluorescence intensity (left) and quantification (right) of ATGL-1::GFP. The scale bar represents 100 µm. **(F)** Localization of ATGL-1::GFP with respect to LDs stained by LipidTOX. White arrows indicate the localization of ATGL-1::GFP on LDs. **(G)** Fluorescence intensity (left) and quantification (right) of ARF-1::RFP. Scale bar represents 100 µm. **(H)** Localization of ARF-1::RFP with respect to LDs stained by LipidTOX (green). White arrows indicate LipidTOX (green) -stained LDs. Data are presented as the mean ± SD. *n*, the number of measured worms for each worm strain. Significant difference between Con and a specific RNAi, ***P < 0.001, ns, no significance, the P values are indicated by two-tailed *t* test (A and C) and one-way ANOVA (E and G). All fluorescence images were captured by high-resolution laser confocal microscopy (ZEISS, Carl LSM800), with the exception of A, B, E, and G taken by ZEISS Axio Imager M2 microscopy. Scale bar represents 1 µm in enlarged panels and 5 µm in others, respectively, unless specifically indicated.

Provided online are four tables. Table S1 shows experimental models: organisms/strains. Table S2 shows the 51 candidate genes. Table S3 shows the RNA-Seq analysis of WT;*let-767*RNAi via pathway enrichment. Table S4 lists proteins interacting with LET-767 detected by IP-MS.